Ideal Optical Flux Lattices

Ophelia Evelyn Sommer
Department of Physics, Harvard University, Cambridge, MA 02138, USA

Nigel R. Cooper
T.C.M. Group, Cavendish Laboratory, University of Cambridge, J.J. Thomson Avenue, Cambridge CB3 0US, United Kingdom

The realization of fractional quantum Hall (FQH) states in cold atomic gases is a long-standing goal in quantum simulation. Established approaches, including rapidly rotating gases and tight-binding lattices, are often hampered by low interaction energies and small many-body energy gaps. While optical flux lattices (OFLs) can achieve higher effective magnetic flux densities, standard two-state configurations generate highly non-uniform fields, and extensions to multi-state systems introduce significant experimental complexity. Here, we present a new paradigm for engineering robust FQH phases in OFLs using only two internal atomic states. We show that the introduction of an additional scalar potential provides a generic mechanism for creating Chern bands that are simultaneously essentially flat and "ideal." These desirable properties arise by tuning lattice parameters to certain N-flat manifolds ($N = 1, 2, \dots$), where the 1-flat manifold shares its origin with certain "magic-angle" conditions familiar from moiré materials. A central result is the design of a dark-state OFL whose adiabatic Hamiltonian is *exactly* of Aharonov-Casher (AC) form. This exact AC equivalence guarantees perfectly flat, exactly ideal Chern bands in the adiabatic limit. This method allows for precise tuning of band flatness and stabilizes both Abelian and non-Abelian FQH phases. Our scheme is compatible with existing experimental capabilities using vector polarizability, opening practical routes to exploring strongly correlated topological physics with cold atoms.

I. INTRODUCTION

One of the long-standing challenges in quantum simulation using cold atomic gases is the realization of fractional quantum Hall (FQH) states. The possibility of using experiments on cold atomic gases to explore FQH states of bosons – in place of the fermions familiar from electronic matter – was first discussed in the context of Bose-Einstein condensates in harmonic trapping potentials, for which Landau level wavefunctions emerge under rapid rotation[1, 2]. Remarkably, the bosonic Laughlin state can be the *exact* ground state at sufficiently high angular momentum[3], due to the short-range nature of typical interatomic interactions. Subsequent theoretical work established the phases of short-range interacting bosons as a function of the Landau level filling factor, ν[4]. In addition to conventional hierarchy/composite fermion states, bosons form unusually stable non-Abelian phases: including the Moore-Read phase[5] at $\nu = 1$[4, 6], and the Read-Rezayi phases[7, 8]. Achieving these FQH phases in experiments using rotating gases is extremely challenging, in part due to the low flux densities and hence low interaction energies. However, this may be mitigated by tight confinement using optical tweezers[9].

One way to increase the interaction energies of FQH states is to place the atoms in tight-binding lattices, engineered (by breaking time-reversal symmetry) to host narrow Chern bands[1]. The Harper-Hofstadter model supports the $\nu = 1/2$ bosonic Laughlin state[10] and $\nu = 1$ Moore-Read state[11], as well as other FQH states that are stabilized by the lattice itself and do not have continuum analogues[12]. Interaction energies are boosted compared to those in rotating gases, but they typically remain small. The state of the art experiments[13] have shown Laughlin correlations for two particles, with a many-body energy gap of order $\sim 1\,\mathrm{Hz}$.

A separate approach to forming Chern bands for cold atoms uses the possibility to couple internal (electronic or magnetic) levels of atoms, to form so-called "optical flux lattices" (OFLs)[14]. The main conceit of OFLs is that they require state-dependent potentials that do not commute at different points in space. In the deep-lattice limit, the energetically preferred internal state at each point in real space forms a texture with a varying direction. The Berry phase associated to this texture becomes an Aharonov-Bohm phase for an emergent magnetic field associated with the residual dynamics, that often persists even in the intermediate-shallow lattice regime. Thus, OFLs stand in stark contrast to deep-lattice tight-binding models, in that they are generally shallow lattice continuum models. As a result, they can operate at higher flux densities boosting the densities at which FQH states can form, and thereby also the associated energy scales.

While the emergent magnetic field in OFLs has a nonzero average, it is typically spatially varying, so these lattices cannot directly reproduce the uniform continuum Landau levels. In particular, if only two internal levels are coupled the local magnetic field must vanish within the unit cell[14], so the field must have very large spatial variations. To mimic continuum Landau levels more closely, OFLs have been proposed using $N > 2$ internal states[15], which converge quickly to the continuum Landau levels with increasing N. However, experimental implementations[16, 17] quickly become more cumbersome, requiring multiple frequencies of the light field to control the various interspecies couplings, which can lead to enhanced losses through light scattering.

In this paper, we take a different approach, and show

how OFLs using just two internal states can be designed to host robust Abelian and non-Abelian FQH phases. We draw on theoretical work inspired by advances in two-dimensional electronic platforms, such as the moiré materials formed from graphene or TMDs. The prevalence of non-trivial band geometry in these platforms has led to a deeper understanding of the general properties of a single-particle band that are desirable in order to stabilize FQH states[18–32]. A prominent notion emerging from these considerations is that of "ideal" bands, which are "vortexable", and consequently allow for the appearance of exact FQH states for short-range interactions, generalizing the Laughlin state in the lowest Landau level to exact states in these bands.

Our principal result is to present a generic mechanism for creating essentially flat and ideal Chern $|C| = 1$ bands, upon introducing an additional scalar potential to OFLs. This additional scalar potential can be used to tune the flatness of the band to a high precision. These flat bands host fractional quantum Hall phases in the presence of repulsive interactions, and can be realized with currently existing experimental tools in optical lattices using vector polarizability.

A central result within this framework is the construction of a dark-state OFL whose adiabatic Hamiltonian is *exactly* of Aharonov-Casher (AC) form (see Sec. IV B). While the AC Hamiltonian has served as a theoretical ideal for flat bands [32–34], prior realizations have only approximated this structure. The dark-state OFL constructed here achieves it exactly in the adiabatic limit, yielding perfectly flat, exactly ideal Chern bands as an analytical result rather than a numerical observation. This constitutes a physically realizable benchmark for ideal band physics, and offers a tunable, well-characterized platform in which the AC limit is achieved precisely.

The outline of the paper is as follows. In Sec. II we provide background on optical flux lattices, emphasizing their description as reciprocal space tight-binding models. We then describe the concepts of ideality in Sec. III, and explain how to use these to design ideal OFLs. We provide explicit examples of these design principles in Sec. IV, including also for dark-state optical flux lattices. In Sec. V, we demonstrate their utility for stabilizing Abelian and non-Abelian FQH states.

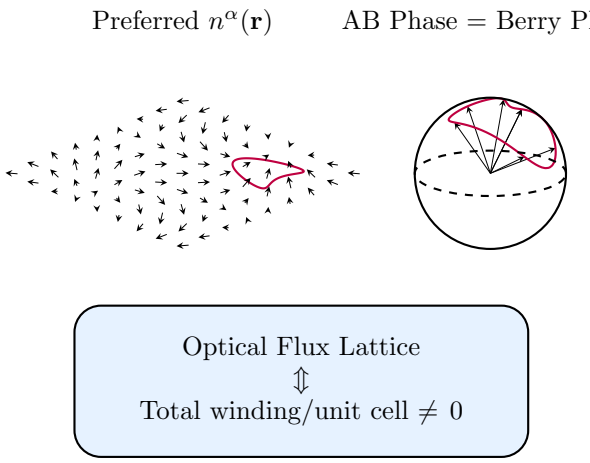


FIG. 1. Graphical illustration of the connection between the low-energy spinor texture and the effective magnetic field. The Aharonov-Bohm (AB) phase picked up upon parallel transport of the emergent scalar particle is the Berry phase of the spinor texture.

II. BACKGROUND ON OPTICAL FLUX LATTICES

A. Real Space Viewpoint

Optical lattices are created by coupling atoms to lasers that transfer momentum. For optical flux lattices, we further allow the lasers to change the internal state of the atom. Let the center-of-mass position of the atom be denoted $\mathbf{r}$, the atomic mass M, and label the manifold of internal energy levels that are coupled resonantly by the lasers $|\alpha\rangle$. Throughout, we consider atoms whose motion is restricted to two dimensions, the xy plane, for example by tight confinement along z, so that $\mathbf{r} = (x, y)$ and all derivatives are in-plane. We will consider this manifold to be a subset of the ground-state manifold of the atom, and ignore finite lifetime effects. Upon eliminating the photon dynamics by going into a rotating frame, the dynamics for the atom are governed by the familiar sum of kinetic and potential energy $\hat{V} = \sum_{\alpha\beta} V^\alpha_\beta(\mathbf{r})\,|\alpha\rangle\langle\beta|$ of a spinor particle

$$\hat{H} = -\frac{\nabla^2_{\mathbf{r}}}{2M}\hat{1} + \hat{V}(\mathbf{r})\,. \tag{1}$$

Despite atomic neutrality, this Hamiltonian can give rise to a lowest band similar to a Landau level [35–37]. The key to understanding this is the spinor nature of the particle, and it is particularly clear in the adiabatic deep-lattice limit $M \to \infty$. In this limit, the Hamiltonian reduces to the potential energy $\hat{V}(\mathbf{r})$. The low-energy manifold consists of the ground state of $V^\alpha_\beta(\mathbf{r})$ for each $\mathbf{r}$, which forms a spinor texture $n^\alpha(\mathbf{r})$. Consider now including the leading $1/M$ corrections to the dynamics, which amounts to projecting (1) to the subspace of adiabatic wavefunctions of the form $\langle \mathbf{r}, \alpha|\psi\rangle = \psi^\alpha(\mathbf{r}) = b(\mathbf{r})n^\alpha(\mathbf{r})$ where $b(\mathbf{r})$ is an arbitrary scalar wavefunction. Since $n^\alpha(\mathbf{r})$ is fixed, the dynamics are purely those of the scalar $b(\mathbf{r})$. Under an infinitesimal translation the total wavefunction picks up a Berry phase[38] from the change in the spinor direction. This manifests as an emergent background gauge field acting on $b(\mathbf{r})$, which is evident from projecting the momentum to the space of adiabatic wavefunctions

$$-\mathrm{i}\bar{n}_\alpha(\mathbf{r})\nabla_{\mathbf{r}}\psi^\alpha(\mathbf{r}) = [-\mathrm{i}\nabla_{\mathbf{r}} - \mathrm{i}\bar{n}_\alpha(\mathbf{r})\nabla_{\mathbf{r}}n^\alpha(\mathbf{r})]b(\mathbf{r})\,. \tag{2}$$

Clearly this is the same form as a scalar particle in the presence of a magnetic field with vector potential $\mathbf{A}_{\text{texture}} = \mathrm{i}\bar{n}_\alpha(\mathbf{r})\nabla_{\mathbf{r}}n^\alpha(\mathbf{r})$, or equivalently magnetic field

$$B_{\text{texture}}(\mathbf{r}) = \mathrm{i}\nabla_{\mathbf{r}}\bar{n}_\alpha(\mathbf{r}) \wedge \nabla_{\mathbf{r}}n^\alpha(\mathbf{r})\,. \tag{3}$$

Here $\mathbf{a} \wedge \mathbf{b} \equiv a_x b_y - a_y b_x$, so that, for this two-dimensional geometry, the effective magnetic field is a scalar: $B_{\rm texture} = \mathbf{e}_z \cdot (\nabla_{\mathbf{r}} \times \mathbf{A}_{\rm texture})$ is the component perpendicular to the plane. The Berry phase of the spinor texture becomes the Aharonov-Bohm phase[39] of the effective magnetic field felt by $b(\mathbf{r})$[14, 35, 40], and the astute reader will recognize equation (3) as the expression for the Berry curvature of $n^\alpha(\mathbf{r})$. The Hamiltonian governing b in the adiabatic limit takes the form

$$H^{\rm adi} = \frac{(-\mathrm{i}\nabla_{\mathbf{r}} - \mathbf{A}_{\rm texture})^2}{2M} + \frac{D(\mathbf{r})}{2M} + \bar{n}_\alpha V_\beta^\alpha n^\beta \quad (4)$$

where $D(\mathbf{r}) = \nabla\bar{n}_\alpha(\delta_\beta^\alpha - n^\alpha\bar{n}_\beta)\nabla n^\beta$ is the trace of the Fubini-Study metric of the texture. This adiabatic Hamiltonian is valid whenever the low-energy dynamics can be projected along a spin texture. This is evidently justified in deep lattices, but even when V_β^α is comparable to the typical kinetic energy, there are a plethora of examples where this holds approximately.

An optical flux lattice (OFL) is defined to be an optical lattice whose low-energy subspace has a texture $n^\alpha(\mathbf{r})$ with effective magnetic field $B_{\rm texture}$ of nonzero average flux.

Perhaps the simplest example – for a two-level system – is the triangular OFL introduced in Ref. [14], for which

$$\hat{V}_{\rm tri}(\mathbf{r}) = \sum_{i=1}^{3} \hat{\sigma}_i \cos(\mathbf{q}_i \cdot \mathbf{r}) \,, \quad (5)$$

where $\hat{\sigma}_{i=1,2,3}$ are the Pauli matrices, and $\mathbf{q}_i$ are three in-plane momentum at 120° to each other. We define them as

$$\mathbf{q}_i \equiv q\mathbf{e}_x \cos\tfrac{2\pi i}{3} + q\mathbf{e}_y \sin\tfrac{2\pi i}{3} \quad (6)$$

in terms of the orthogonal unit vectors $\mathbf{e}_{x,y}$ and the overall momentum scale q. It is readily found that $\hat{V}_{\rm tri}(\mathbf{r})$ is gapped at all positions, and the dressed state wraps the Bloch sphere to give nonzero flux of $B_{\rm texture}(\mathbf{r})$ through the periodic real-space cell. The real-space lattice is triangular. Moreover, the observables of the texture have a higher translational symmetry than the potential itself. A translation by half a lattice vector of $\hat{V}_{\rm tri}$ can be compensated by a rotation of the spin, which leaves $B_{\rm texture}(\mathbf{r})$ and $D(\mathbf{r})$ invariant. Consequently $B_{\rm texture}(\mathbf{r})$ and $D(\mathbf{r})$ are periodic on a smaller cell, which encloses just π flux of $B_{\rm texture}(\mathbf{r})$. (This is discussed further in Sec. II C.)

Practical implementations for OFLs in cold atomic gases are likely to employ two-photon Raman coupling. A simple form of OFL using two-photon coupling was proposed in Ref. [41]. This uses three in-plane beams at frequency ω_L along directions $\mathbf{q}_i$ (6) to form Rabi couplings,

$$\kappa_0 = \kappa\cos\theta \sum_{i=1}^{3} \mathrm{e}^{\mathrm{i}\mathbf{q}_i\cdot\mathbf{r}} \,, \quad (7)$$

$$\kappa_\pm = \frac{\mathrm{i}\kappa\sin\theta}{\sqrt{2}} \sum_{i=1}^{3} \mathrm{e}^{\mathrm{i}\mathbf{q}_i\cdot\mathbf{r}\mp 2\pi\mathrm{i}i/3} \,, \quad (8)$$

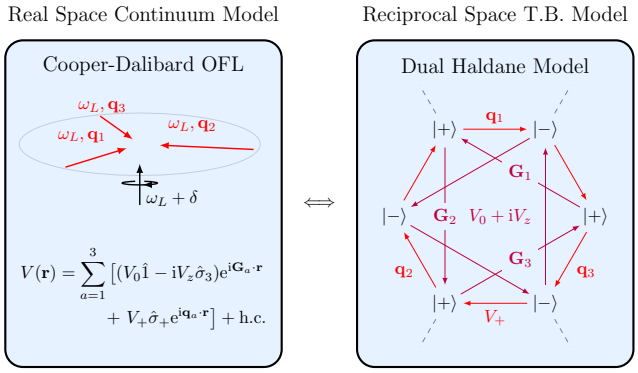


FIG. 2. Illustration of how the two-photon optical flux lattice introduced in Ref. [41] can be viewed as a tight-binding model in reciprocal space, which is equivalent to the Haldane model. All couplings are two-photon processes via the far-detuned electronically excited $J' = 1/2$ states, which are only virtually populated. Interspecies coupling involves one photon at ω_L and one at $\omega_L + \delta$, with momentum transfers $\mathbf{q}_i$. Intraspecies couplings involve two photons at ω_L, with momentum transfers $\mathbf{G}_i = \mathbf{q}_{i+1} - \mathbf{q}_i$.

where κ and θ are parameters, and $\kappa_\pm$ follow from projecting the in-plane polarization $\sin\theta\,\hat{\mathbf{e}}_z\times\hat{\mathbf{q}}_i$ of each beam onto the circular polarization vectors $\mathbf{e}_\pm = \mp(\mathbf{e}_x \pm \mathrm{i}\mathbf{e}_y)/\sqrt{2}$. These are the Rabi couplings for the π ($m = 0$) and $\sigma_\pm$ ($m = \pm$) polarization components of the $J = 1/2 \to J' = 1/2$ optical transition. The lasers are far detuned, so the electronically excited $J' = 1/2$ states are only virtually populated and can be adiabatically eliminated; see Ref. [41] for details. The transition between internal states involves one out-of-plane circularly polarized beam at frequency $\omega_L + \delta$ with spatially uniform coupling κ'_-. [See Fig. 2(a).] From these, the potential is of the form

$$\hat{V}_{2-\rm photon}(\mathbf{r}) = \frac{\kappa_{\rm tot}^2}{3\Delta}\hat{1} + \frac{1}{3\Delta}\left[(|\kappa_-|^2 - |\kappa_+|^2)\hat{\sigma}_3 + \kappa'_-\kappa_0\hat{\sigma}_+ + \bar{\kappa}'_-\bar{\kappa}_0\hat{\sigma}_-\right] , \quad (9)$$

where $\kappa_{\rm tot}^2 = \sum_m |\kappa_m|^2$, $\Delta = \omega_L - \omega_A$ is the detuning of the lasers from the $J = 1/2 \to J' = 1/2$ atomic resonance ω_A, with $|\Delta| \gg |\delta|, |\kappa_m|$, and δ is the Zeeman splitting between the two internal states $|\pm\rangle$, so that the $\omega_L + \delta$ beam together with the π component κ_0 of the in-plane beams drives a resonant Raman coupling between them. Eq. (9) is written in the $\{|+\rangle, |-\rangle\}$ basis, in the rotating frame, with $\hbar = 1$. See Appendix E for details on the polarizability. This again leads to a real-space unit cell that is triangular, in which the Bloch vector wraps the sphere, signaling that there is a net flux per unit cell. However, in this case the minimal translational symmetry encloses 2π flux per unit cell.

B. Designing in reciprocal space

The definition of OFLs, and the above examples, were motivated by the properties in real space. However, given

that optical lattices involve the use of lasers to write in momentum transfers (with or without changes in internal state), it is very instructive to view them in reciprocal space. Indeed, this set of momentum transfers directly constructs a tight-binding model in reciprocal space. In the adiabatic limit, the effective magnetic field is nothing but the Berry curvature of $n^\alpha(\mathbf{r})$. Here the real-space position $\mathbf{r}$ plays the role of the quasi-momentum of the reciprocal-space tight-binding model, so that $n^\alpha(\mathbf{r})$ at a given $\mathbf{r}$ is the lowest-energy eigenstate of the dual model at that quasi-momentum, and taken over all $\mathbf{r}$ it describes the entire lowest band of this reciprocal-space tight-binding model[15]. Hence considering any tight-binding Chern insulator with Hamiltonian $V^\alpha_\beta(\mathbf{k})$, there is a dual optical flux lattice with potential $V^\alpha_\beta(\mathbf{r})$.

To illustrate the reciprocal space mapping, consider the triangular OFL constructed for spin-1/2 fermionic atoms in [41], and defined above, Eq. (9). The interspecies coupling involves one in-plane photon, from the π component κ_0, and one out-of-plane photon from κ'_-. Thus, from (7), it involves momentum transfers of the three $\mathbf{q}_i$. These couplings construct the nearest-neighbor bonds on a honeycomb lattice in reciprocal space, with $|\pm\rangle$ at the two inequivalent sites. The intraspecies couplings involve two in-plane photons, thus giving momentum transfers of $\mathbf{G}_2 = \mathbf{q}_3 - \mathbf{q}_2$ etc. These couplings give the next-nearest-neighbor bonds on the honeycomb lattice. Overall the optical potential of the two-photon OFL of Ref. [41] generates precisely the Haldane model in reciprocal space. See Fig. 2(b). This tight-binding model is in its topological phase, with unit Chern number, consistent with the fact that the corresponding OFL has 2π flux per real space unit cell[41].

This is one of the model potentials that we shall focus on in the rest of the paper. Although it was first introduced in Ref. [41] as a model for spin-1/2 atoms in an optical flux lattice, in light of the connections highlighted above, we shall refer to it as the *dual Haldane model*, and denote the potential as $\hat{V}^{\hexagon}$ to represent the hexagonal lattice in reciprocal space. For generality, we shall add a scalar potential, and write the model potential as

$$\hat{V}^{\hexagon}(\mathbf{r}) = \sum_{a=1}^{3} (V_0\hat{1} - \mathrm{i}V_z\hat{\sigma}_3)\mathrm{e}^{\mathrm{i}\mathbf{G}_a\cdot\mathbf{r}} + V_+\hat{\sigma}_+\mathrm{e}^{\mathrm{i}\mathbf{q}_a\cdot\mathbf{r}} + \mathrm{h.c.}\,, \quad (10)$$

with parameters $V_{0,z,+}$.

Note that the mapping to the dual Haldane model applies only to the optical potential $\hat{V}(\mathbf{r})$ and therefore to the real-space spinor texture; the model of Ref. [41] also includes the kinetic energy term of (1) so its energy bands depend on the ratio of kinetic to potential energies. The kinetic energy is quadratic in momenta, and so the total single-particle energy is obtained by introducing a momentum space 'harmonic oscillator potential', whose minimum is located at the location of the crystal momentum under consideration $\mathbf{k}$. This same model is also an effective Hamiltonian for electrons in a single valley of twisted transition metal dichalcogenide homobilayers[32, 42]. To understand why, it is helpful to think in reciprocal space, as above: the OFL of Cooper and Dalibard [41] is precisely the Haldane model written in reciprocal space – the dual Haldane model considered here – which is the simplest two-state tight-binding model with triangular symmetry and short-range hopping. It is therefore unsurprising that the simplest two-state model describing a single TMD valley, sharing the same symmetry and minimizing the number of wavevector transfers, coincides with it exactly. This identification of the two models shows the power of designing Chern bands in reciprocal space. In moiré materials the overall ratio of kinetic to potential energy is controllable by the twist angle, though the ratio of the potential parameters is determined chemically, and may also depend on the twist angle through lattice relaxation. As each potential parameter is individually tunable in cold atomic gases, the dual Haldane model is far more flexible in this setting, and furthermore comparatively easy to characterize. In particular, in the general model (10) we have added the freedom to tune the scalar potential V_0 separately from the other couplings.

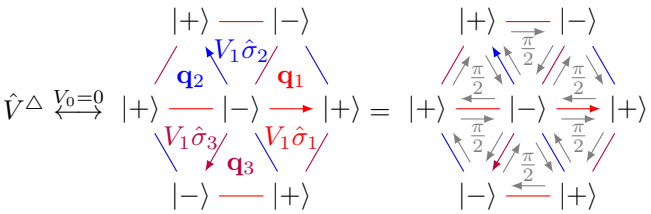


FIG. 3. The momentum space couplings of $\hat{V}^{\triangle}$ in the absence of the scalar potential form a nearest-neighbor $\pi/2$ flux triangular lattice.

Similarly, we adapt the potential of the triangular model (5) to include a scalar potential V_0, beyond the case $V_0 = 0$ considered in [14]. We call this the *dual triangular model* – strictly it is a nearest-neighbor triangular lattice in reciprocal space at $\pi/2$ flux (see Fig. 3). We write it in the form

$$\hat{V}^{\triangle}(\mathbf{r}) = \sum_{a=1}^{3} V_1\hat{\sigma}_a\mathrm{e}^{\mathrm{i}\mathbf{q}_a\cdot\mathbf{r}} + V_0\hat{1}\mathrm{e}^{2\mathrm{i}\mathbf{q}_a\cdot\mathbf{r}} + \mathrm{h.c.}\,. \quad (11)$$

Finally, a square version of this model, the *dual square model*, can be constructed similarly using next-nearest-neighbor momentum transfers. Let $\tilde{\mathbf{q}}_{1,2,3,4}$ be $\pi/2$-rotated momenta of equal magnitude, $\tilde{\mathbf{G}}_1 = \tilde{\mathbf{q}}_2 - \tilde{\mathbf{q}}_1$ along with cyclic permutations, and $\hat{\sigma}^\perp_a = \hat{\sigma}_{a \bmod 2}$. The potential we consider adds a scalar lattice to the model in [14, 43] and takes the form:

$$\hat{V}^{\square}(\mathbf{r}) = \sum_{a=1}^{4} V_+\hat{\sigma}^\perp_a\mathrm{e}^{\mathrm{i}\tilde{\mathbf{q}}_a\cdot\mathbf{r}} + V_z\hat{\sigma}_3\mathrm{e}^{\mathrm{i}\tilde{\mathbf{G}}_a\cdot\mathbf{r}} + V_0\hat{1}\mathrm{e}^{2\mathrm{i}\tilde{\mathbf{G}}_a\cdot\mathbf{r}} \quad (12)$$

where $V_{0,z,+}$ are tunable potential strengths. Strictly this dual square lattice is a next-nearest-neighbor square lattice in reciprocal space at $\pi/2$ flux per triangular plaquette.

C. Translational Symmetries

We shall make much use of symmetries in later sections of the paper. It is therefore important to pause to consider in detail the symmetries of the three lattices just presented.

Arising from standing beams of light in a periodic interference pattern, the potential is genuinely periodic. Nevertheless, a finer translational symmetry can often be found by letting the translation operators act on the spinor degrees of freedom.

For the dual triangular (square) model, the minimal unit cell under which $\hat{V}^{\triangle}$ ($\hat{V}^{\square}$) is periodic has reciprocal lattice $\Lambda^{\star}_{\rm pot} = 2\mathbf{q}_1\mathbb{Z} \oplus 2\mathbf{q}_2\mathbb{Z}$ ($\Lambda^{\star}_{\rm pot} = 2\tilde{\mathbf{q}}_1\mathbb{Z} \oplus 2\tilde{\mathbf{q}}_2\mathbb{Z}$). Let $\mathbf{R}_{1,2}$ be the dual basis of $\Lambda_{\rm pot}$, then the translation operators $\hat{T}_1 = \mathrm{e}^{\mathbf{R}_1\cdot\nabla}\hat{\sigma}_2, \hat{T}_2 = \mathrm{e}^{\mathbf{R}_2\cdot\nabla}\hat{\sigma}_1$ are symmetries $\hat{T}_a\hat{H} = \hat{H}\hat{T}_a$. However, they only furnish a projective representation of the translation group, as they do not mutually commute $\hat{T}_1\hat{T}_2 = -\hat{T}_2\hat{T}_1$. This is because the *real space* unit cell of $\Lambda_{\rm pot}$ only encloses π flux. By doubling the unit cell, a commuting translation algebra is generated by $\hat{T}_1^2, \hat{T}_2$[14]. To compute a band structure we therefore use the lattice $\Lambda = 2\mathbf{R}_1\mathbb{Z} \oplus \mathbf{R}_2\mathbb{Z}$. Nevertheless, the finer true symmetry makes its existence felt by restricting the possible non-vanishing Fourier component of observables. Noting the *real space* flux and 6-fold C_6 (4-fold C_4) rotational symmetry of $\Lambda^{\star}$, we refer to this situation as C_6 π-flux (C_4 π-flux) symmetry.

For the dual Haldane model, $\hat{V}^{\hexagon}$, the finest translation symmetry is commuting and has C_6 symmetric reciprocal lattice $\Lambda^{\star} = \Lambda^{\star}_{\rm pot} = \mathbf{G}_1\mathbb{Z} \oplus \mathbf{G}_2\mathbb{Z}$. We call this C_6 2π-flux symmetry, and the analogous situation for a square lattice would be C_4 2π-flux symmetry.

III. IDEALITY

Having discussed several examples of OFLs, let us return to the adiabatic Hamiltonian (4). A flat Chern band is evidently furnished from the Landau levels when the magnetic field and potential $\frac{D}{2M} + \bar{n}_\alpha V^\alpha_\beta n^\beta$ are both uniform. Perhaps surprisingly, as was recognized in [33], and later in the context of adiabatic moiré bands[32, 34], a flat lowest band can survive a non-uniform magnetic field $B_{\rm texture}(\mathbf{r})$ with the same average, when the potential takes the value $\frac{D}{2M} + \bar{n}_\alpha V^\alpha_\beta n^\beta = -\frac{B_{\rm texture}}{2M}$. The Hamiltonian then reduces to the Aharonov-Casher (AC) form:

$$H^{\rm AC} = \frac{[-\mathrm{i}\nabla_{\mathbf{r}} - \mathbf{A}_{\rm texture}(\mathbf{r})]^2}{2M} - \frac{B_{\rm texture}(\mathbf{r})}{2M}\,. \tag{13}$$

To see how this occurs, let us introduce the following notation to draw similarities with the Landau levels. (A more complete review is given in Appendix C.) Denote the unit cell area of Λ containing 2π flux by $2\pi\ell_B^2$, and the associated cyclotron frequency $\omega_c = (M\ell_B^2)^{-1}$. We use the complexified coordinate $z = x + \mathrm{i}y$, while the complexified kinetic momentum for the corresponding uniform field (in symmetric gauge) is $\pi = -\mathrm{i}(\partial_x - \mathrm{i}\partial_y) + \mathrm{i}\bar{z}/2\ell_B^2$. We will also need the momenta of opposite chirality, which can be considered the 'guiding-center' momenta, $\tilde{\pi} = \pi - \mathrm{i}\bar{z}/\ell_B^2$. A non-uniform field with average ℓ_B^{-2} can be described by the complexified vector potential $\mathcal{A} = \mathrm{i}\bar{n}_\alpha(\partial_x + \mathrm{i}\partial_y)n^\alpha = \mathrm{i}z/2\ell_B^2 + \delta\mathcal{A}$. Thus the AC Hamiltonian can be rewritten as

$$H^{\rm AC} = \frac{(\pi - \delta\bar{\mathcal{A}})(\pi^\dagger - \delta\mathcal{A})}{2M}\,. \tag{14}$$

This Hamiltonian naturally has zero modes equal in quantity to the number of solutions to

$$[\pi^\dagger - \delta\mathcal{A}]b(\mathbf{r}) = 0. \tag{15}$$

When $\delta\mathcal{A} = 0$, this is nothing but the usual lowest Landau level (LLL) condition, with solutions for each crystal momentum $\mathbf{k}$ in the Brillouin zone of $\Lambda^{\star}$ given by

$$\langle\mathbf{r}|\mathbf{k}\rangle = \mathcal{N}\sigma(z - \mathrm{i}\ell_B^2 k)\mathrm{e}^{-(\ell_B^{-2}|z|^2 + \ell_B^2|k|^2)/4 + \mathrm{i}\bar{k}z/2}, \tag{16}$$

where σ is the modified Weierstrass σ-function[44], $k = k_x + \mathrm{i}k_y$, and $\mathcal{N}$ is a normalization constant. Furthermore, whenever $\delta\mathcal{A}$ corresponds to a magnetic field modulation $\delta B_{\rm texture} = B_{\rm texture} - \ell_B^{-2}$ with vanishing average, the generic solution to (15) takes the form of density modulated lowest Landau levels

$$b_{\mathbf{k}}(\mathbf{r}) = \mathrm{e}^{\phi(\mathbf{r})}\,\langle\mathbf{r}|\mathbf{k}\rangle\,; \qquad \pi^\dagger\phi = \delta\mathcal{A}\,. \tag{17}$$

In the Coulomb gauge $\nabla_{\mathbf{r}}\cdot\mathbf{A}_{\rm texture} = 0$ the density modulation e^{ϕ} is the Kähler potential for the magnetic field modulation

$$-\nabla^2\phi = \delta B_{\rm texture}(\mathbf{r})\,. \tag{18}$$

The manifold of zero modes forms a flat band with Chern number $\mathcal{C} = -1$. Beyond being a flat Chern band, the LLL is remarkable for the ability to attach vortices within it, so that $b(\mathbf{r}) \mapsto zb(\mathbf{r})$ does not cause any excitation. Chern bands for which vortex attachment is possible are known as ideal or vortexable[18, 19]; in the remainder of this paper we use the term "ideal" (and "ideality") throughout. Wavefunctions belonging to many fractional quantum Hall phases in the LLL have exact parent Hamiltonian given by various zero-range repulsive interactions, with respect to which they have zero energy. For such parent interactions, ideal bands that are flat also give rise to zero energy ground states in the same phase as the LLL. For scalar particles with $\mathcal{C} = -1$ (and 2π flux per unit cell), the AC wavefunctions (17) exhaust the possibilities for ideal wavefunctions[20].

Instead of approaching the design of OFLs with a view towards mimicking a uniform field, a natural path to flat ideal bands is AC Hamiltonian mimicry. For the general case on which we first focus, we will not be able to find an exact AC Hamiltonian. Nevertheless, we shall show that perturbations to an AC Hamiltonian are well behaved, even when they are comparable in size to the

typical gap $\sim \omega_c$. Including an amplitude modulated spinor $\chi^\alpha(\mathbf{r}) = n^\alpha(\mathbf{r})e^{\phi(\mathbf{r})}$, a $\mathcal{C} = -1$ ideal band in an OFL has wavefunction

$$\psi^\alpha_{\mathbf{k}}(\mathbf{r}) = \chi^\alpha(\mathbf{r})\,\langle \mathbf{r}|\mathbf{k}\rangle\ . \tag{19}$$

A useful practical criterion for ideality is saturating the trace inequality, which we now describe. To any wavefunction with crystal momentum $\mathbf{k}$ there is a periodic Bloch wavefunction of the form $\langle \mathbf{r}\alpha|u_{\mathbf{k}}\rangle = e^{-i\mathbf{k}\cdot\mathbf{r}}\psi^\alpha_{\mathbf{k}}(\mathbf{r})$. From this we may compute the Berry curvature $\Omega(\mathbf{k}) = i\,\langle\nabla_{\mathbf{k}}u_{\mathbf{k}}|\wedge|\nabla_{\mathbf{k}}u_{\mathbf{k}}\rangle$ and Fubini-Study metric $g^{ab}(\mathbf{k}) = \langle\nabla^a_{\mathbf{k}}u_{\mathbf{k}}|(1-|u_{\mathbf{k}}\rangle\langle u_{\mathbf{k}}|)|\nabla^b_{\mathbf{k}}u_{\mathbf{k}}\rangle$. For any band $\mathrm{Tr}\,g(\mathbf{k}) \geq |\Omega(\mathbf{k})|$ with equality for all $\mathbf{k}$ only if the band is ideal[18]. Noting that $\int d^2\mathbf{k}\,\Omega(\mathbf{k}) = 2\pi\mathcal{C}$, a natural measure of deviation from ideality is the trace violation

$$T = \left[\frac{1}{2\pi}\int d^2\mathbf{k}\,\mathrm{Tr}\,g(\mathbf{k})\right] - |\mathcal{C}| \geq 0\,, \tag{20}$$

which takes the value $2n$ for the nth Landau level[31], see Appendix C 2 for a derivation. For comparison with a different measure of ideality deviation used in [45] see Appendix C 3.

A. Form factor filtering

With the preparation of the previous sections, let us wrest nearly flat and ideal bands from the flexibility afforded by the optical lattice potential. The key principle that will permit the near-flat ideal Chern bands in general cases is that the size of the cyclotron orbits significantly suppresses small-scale variations, as measured by the magnetic form factor

$$I_{\mathbf{G}\in\Lambda^\star}(\mathbf{k}) = \langle\mathbf{k}|e^{i\mathbf{G}\cdot\mathbf{r}}|\mathbf{k}\rangle \tag{21}$$

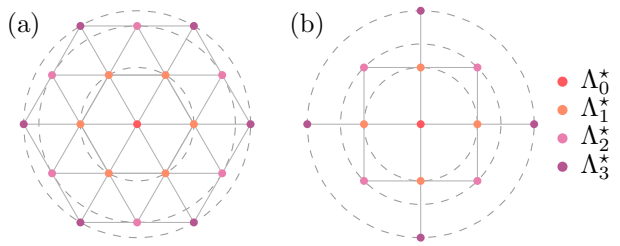
$$= \langle\mathbf{k}|e^{\ell_B^2 G(\pi-\bar\pi)/2+\ell_B^2\bar G(\bar\pi^\dagger-\pi^\dagger)/2}|\mathbf{k}\rangle \tag{22}$$

$$= e^{\ell_B^2[i\mathbf{G}\wedge\mathbf{k}-\mathbf{G}^2/4]}\begin{cases}+1 & \mathbf{G}/2\in\Lambda^\star\\ -1 & \text{otherwise}\end{cases} \tag{23}$$

This suppression acts as a strong low-momentum filter on many quantities of interest. The strength of this filter is controlled by the symmetry allowed reciprocal lattice vectors, which can naturally be ordered into shells of increasing momentum magnitude. For the models which we seek to study, we note the relevant magnitudes in Table I.

B. Ideal perturbation theory

To go beyond the Aharonov-Casher limit of ideal wavefunctions as zero modes of (13), a non-unitary basis change is illuminating. Instead of working with the typical Bloch basis, we factorize a LLL piece, so that a generic wavefunction $\psi^\alpha_{\mathbf{k}}(\mathbf{r})$ is specified by the spinor $\chi^\alpha_{\mathbf{k}}(\mathbf{r})$ as



	Shell	$\Lambda^\star_1$	$\Lambda^\star_2$	$\Lambda^\star_3$
C_6	2π-flux $\lvert I_{\mathbf{G}}\rvert$	1.6×10^{-1}	4.3×10^{-3}	7.1×10^{-4}
C_6	π-flux $\lvert I_{\mathbf{G}}\rvert$	2.7×10^{-2}	1.9×10^{-5}	5.0×10^{-7}
C_4	2π-flux $\lvert I_{\mathbf{G}}\rvert$	2.1×10^{-1}	4.3×10^{-2}	1.9×10^{-3}
C_4	π-flux $\lvert I_{\mathbf{G}}\rvert$	4.3×10^{-2}	1.9×10^{-3}	3.5×10^{-6}

TABLE I. Illustration of momentum shells for (a) C_6-symmetric and (b) C_4-symmetric lattices. Form factors (23) for the inner three shells are tabulated for models with 2π and π-flux symmetries.

$\psi^\alpha_{\mathbf{k}}(\mathbf{r}) = \chi^\alpha_{\mathbf{k}}(\mathbf{r})\,\langle\mathbf{r}|\mathbf{k}\rangle$. In this basis, the space of ideal wavefunctions are those where $\chi_{\mathbf{k}}$ is momentum independent. Consider a situation where the ideal wavefunction (19) describes the lowest band. It is generically dispersive, as can be computed by the Rayleigh quotient

$$E_{\mathbf{k}}[\chi^\alpha] = \frac{\int d\mathbf{r}\ |\langle\mathbf{r}|\mathbf{k}\rangle|^2\left[\frac{1}{2M}|\tilde\pi^\dagger\chi^\alpha|^2 + \bar\chi_\alpha V^\alpha_\beta\chi^\beta\right]}{\int d\mathbf{r}\ |\langle\mathbf{r}|\mathbf{k}\rangle|^2\bar\chi_\alpha\chi^\alpha} \tag{24}$$

$$= \frac{\sum_{\mathbf{G}} I_{\mathbf{G}}(\mathbf{k})\left[\frac{1}{2M}|\tilde\pi^\dagger\chi^\alpha|^2 + \bar\chi_\alpha V^\alpha_\beta\chi^\beta\right]_{\mathbf{G}}}{\sum_{\mathbf{G}} I_{\mathbf{G}}(\mathbf{k})[\bar\chi_\alpha\chi^\alpha]_{\mathbf{G}}} \tag{25}$$

where the notation $[\cdot]_{\mathbf{G}}$ is shorthand for the $\mathbf{G}$ Fourier component of the bracketed quantity. The Gaussian decay of $|I_{\mathbf{G}}|$ ensures that the band can be made exponentially flat in the number of tuning parameters of χ^α. To see this, imagine tuning the Fourier components of the numerator and denominator for the N innermost shells $\mathbf{G}\in\Lambda_{0,1,2,\ldots N}$ to have a common ratio

$$E_0 = \left[\frac{1}{2M}|\tilde\pi^\dagger\chi^\alpha|^2 + \bar\chi_\alpha V^\alpha_\beta\chi^\beta\right]_{\mathbf{G}}/[\bar\chi_\alpha\chi^\alpha]_{\mathbf{G}}. \tag{26}$$

Then the first term that causes dispersion is suppressed by $|I_{\mathbf{G}\in\Lambda^\star_{N+1}}|$ compared to the typical energy scale. As long as the potential is at most comparable to ω_c, we expect a bandwidth comparable to $\omega_c|I_{\mathbf{G}\in\Lambda^\star_{N+1}}|$, which decays extremely quickly with N as seen in Table I. Let us refer to this situation as an N-flat band, and the manifold of model parameters on which this is achieved, the N-flat manifold. In a similar discussion, focused on the adiabatic limit for the dual Haldane model, finding a 1-flat manifold was taken as the 'magic angle' condition for twisted transition metal dichalcogenides[34]. The power of optical lattices in cold gases is that one can shape the potential with tuning parameters, so as to reach the 1- or 2-flat regimes, or potentially beyond. Reaching a higher

N-flat condition requires tuning additional, independent Fourier harmonics of the scalar potential. This does not require additional laser beams: as illustrated for the dual Haldane model in App. B, the extra harmonics can instead be added as extra frequency tones on the beams already present, for example using an acousto-optic or electro-optic modulator. Since these tones need only contribute to the scalar potential, they can also be far-detuned, and so do not add appreciably to the photon scattering budget.

This dispersion estimate is only reliable when the band is similarly close to ideality, otherwise the dispersion would be dominated by the $\mathbf{k}$ dependence of the true χ^α. To understand this dependence, consider the reformulation of the genuine eigenvalue equation in terms of the spinor $\chi^\alpha_{n\mathbf{k}}$ which depends on the band index n and the crystal momentum $\mathbf{k}$:

$$\begin{aligned} E_{n\mathbf{k}}\chi^\alpha_{n\mathbf{k}} &= \tilde{H}^\alpha_\beta \chi^\beta_{n\mathbf{k}} + \hat{\zeta}_{\mathbf{k}}\chi^\alpha_{n\mathbf{k}} \qquad (27)\\ &= \left(\frac{\tilde{\pi}\tilde{\pi}^\dagger}{2M}\delta^\alpha_\beta + V^\alpha_\beta\right)\chi^\beta_{n\mathbf{k}} - \frac{\mathrm{i}}{M}\hat{\zeta}(z-\mathrm{i}\ell_B^2 k)\tilde{\pi}^\dagger\chi^\alpha_{n\mathbf{k}} \end{aligned}$$

where we have defined the $\mathbf{k}$-independent operator

$$\tilde{H}^\alpha_\beta \equiv \frac{\tilde{\pi}\tilde{\pi}^\dagger}{2M}\delta^\alpha_\beta + V^\alpha_\beta(\mathbf{r})\,, \qquad (28)$$

which contains the full potential and the kinetic energy of the guiding-center momenta, and the $\mathbf{k}$-dependent operator $\hat{\zeta}_{\mathbf{k}} \equiv -\frac{\mathrm{i}}{M}\hat{\zeta}(z-\mathrm{i}\ell_B^2 k)\tilde{\pi}^\dagger$, which contains all the $\mathbf{k}$ dependence of the eigenvalue problem. Here $\hat{\zeta}(z) = \zeta(z) - \bar{z}/2\ell_B^2 = -\mathrm{i}\sum_{\mathbf{G}\neq\mathbf{0}}\frac{\mathrm{e}^{\mathrm{i}\mathbf{G}\cdot\mathbf{r}}}{\ell_B^2 G}$ is the periodic completion of the Weierstrass ζ function[44]. We warn that $\hat{\zeta}$ has poles at the lattice points, arising from the zeros of $|\langle\mathbf{r}|\mathbf{k}\rangle|^2$. This eigenvalue equation may be readily implemented numerically using the matrix elements computed in Appendix C 1.

In an ideal band, the same spinor χ^α is a solution to equation (27) for all $\mathbf{k}$, hence also the $\mathbf{k}$ average thereof

$$E_\star\chi^\alpha = \tilde{H}^\alpha_\beta\chi^\beta\,. \qquad (29)$$

We take the solution of this equation to be our ansatz for the optimal ideal wavefunction away from the AC limit. This is especially reasonable since χ^α also minimizes the $\mathbf{k}$ averaged energy of the lowest band (25), albeit the average with weighting factor $w(\mathbf{k}) = \int \mathrm{d}\mathbf{r}\ |\langle\mathbf{r}|\mathbf{k}\rangle|^2\bar{\chi}_\alpha\chi^\alpha$. The uniformity of this weighting factor is directly controlled by the Berry curvature distribution $\Omega(\mathbf{k}) = -\ell_B^2 + \nabla^2_{\mathbf{k}}\log w(\mathbf{k})$[18], being the Kähler potential for its modulation. The benefit of the aforementioned perspective, is that the perturbation theory about ideality is well controlled. Let U be the characteristic size of the energetic perturbation from ideality $\langle\mathbf{k}|\bar{\chi}_{m\mathbf{k}}\hat{\zeta}_{\mathbf{k}}\chi_{n\mathbf{k}}|\mathbf{k}\rangle$; elementary perturbation theory then determines the resulting admixture of excited bands into the ideal wavefunction, order by order in U/ω_c.

Expanding the ideal wavefunction in the actual eigenbasis $\chi^\alpha = \sum_{n=0}^\infty c_n(\mathbf{k})\chi^\alpha_{n\mathbf{k}}$ we may estimate the overlap with the lowest band $c_0(\mathbf{k})$ by neglecting the mixing between excited states. This amounts to letting $c_n(\mathbf{k}) = c_0(\mathbf{k})\frac{\langle\mathbf{k}|\bar{\chi}_{n\mathbf{k}}\tilde{H}\chi_{0\mathbf{k}}|\mathbf{k}\rangle}{E_\star - \langle\mathbf{k}|\bar{\chi}_{n\mathbf{k}}\tilde{H}\chi_{n\mathbf{k}}|\mathbf{k}\rangle}$. The denominator is essentially the difference in energy between the 0th and nth band, which generically grows linearly in n. The numerator by contrast is strongly suppressed by the form factor since

$$\begin{aligned} \langle\mathbf{k}|\bar{\chi}_{n\mathbf{k}}\tilde{H}\chi_{0\mathbf{k}}|\mathbf{k}\rangle &= -\langle\mathbf{k}|\bar{\chi}_{n\mathbf{k}}\hat{\zeta}_{\mathbf{k}}\chi_{0\mathbf{k}}|\mathbf{k}\rangle \qquad (30)\\ &= \frac{\mathrm{i}}{M}\sum_{\mathbf{G}\in\Lambda}\bar{G}I_{\mathbf{G}}(\mathbf{k})[\bar{\chi}_{n\mathbf{k}}\tilde{\pi}^\dagger\chi_{0\mathbf{k}}]_{\mathbf{G}} \qquad (31)\end{aligned}$$

Recall that the quantity $[\bar{\chi}_{n\mathbf{k}}\tilde{\pi}^\dagger\chi_{0\mathbf{k}}]_{\mathbf{G}}$ vanishes in the AC limit. If U is the characteristic energy scale associated with the deviation therefrom, equation (29) implies that χ is modified at order U/ω_c. Neglecting numerical constants except for the Gaussian we generically expect $|c_0(\mathbf{k})|^2/w(\mathbf{k}) \sim 1 - \mathrm{e}^{-\ell_B^2\mathbf{G}_1^2/2}U^2/\omega_c^2$ where $\mathbf{G}_1 \in \Lambda_1^\star$. By contrast the overlap between the AC and optimal χ is $\sim 1 - U^2/\omega_c^2$. This suggests that the shape of the ideal wavefunction is easily perturbed, but near-ideality (overlap with an ideal wavefunction comparable to $1-|I_{\mathbf{G}\in\Lambda_1^\star}|^2$) is considerably more robust. Taking this effect into account, the true lowest band dispersion $E_{0\mathbf{k}}$ is

$$E_{0\mathbf{k}} = E_{\mathbf{k}} + \sum_{n>0}\frac{(E_{\mathbf{k}} - E_{n\mathbf{k}})|\langle\mathbf{k}|\bar{\chi}_{n\mathbf{k}}\hat{\zeta}_{\mathbf{k}}\chi_{0\mathbf{k}}|\mathbf{k}\rangle|^2}{(E_\star - \langle\mathbf{k}|\bar{\chi}_{n\mathbf{k}}\tilde{H}\chi_{n\mathbf{k}}|\mathbf{k}\rangle)^2} \qquad (32)$$

The difference from the ideal estimate is suppressed to have order of magnitude $U^2|I_{\mathbf{G}\in\Lambda_1^\star}|^2/\omega_c$. Even when $U\sim\omega_c$ this is comparable to the 1-flat dispersion, while the quadratic U dependence hints that sufficiently close to an AC limit, the 2-flat, and beyond, manifold may be achievable.

Consider an optical lattice model with tunable potential parameters $V_0, V_1, \ldots$ controlling the lattice potential at various shells. If there is some parameter point $V_0^\star, V_1^\star, \ldots$ for which the model forms a nearly ideal OFL, our analysis indicates the following features

1. The model is nearly ideal in a parameter region of extent comparable to ω_c surrounding $V_0^\star, V_1^\star, \ldots$.
2. If a model possesses the same rotational symmetry as the lattice $\Lambda^\star$, a codimension-N submanifold is N-flat, though for $N>1$ this may only be resolvable sufficiently close to an AC limit.
3. Since it is possible to reach N-flatness by approaching the AC limit for any spinor texture, we expect that N-flatness can be achieved by adding only additional scalar lattice parameters to an OFL.

IV. EXAMPLE IDEAL OPTICAL FLUX LATTICES

Our analysis provides a lens through which to search the parameter space of the models we constructed in Sec. II B. Consider first the dual triangular model (11) and dual

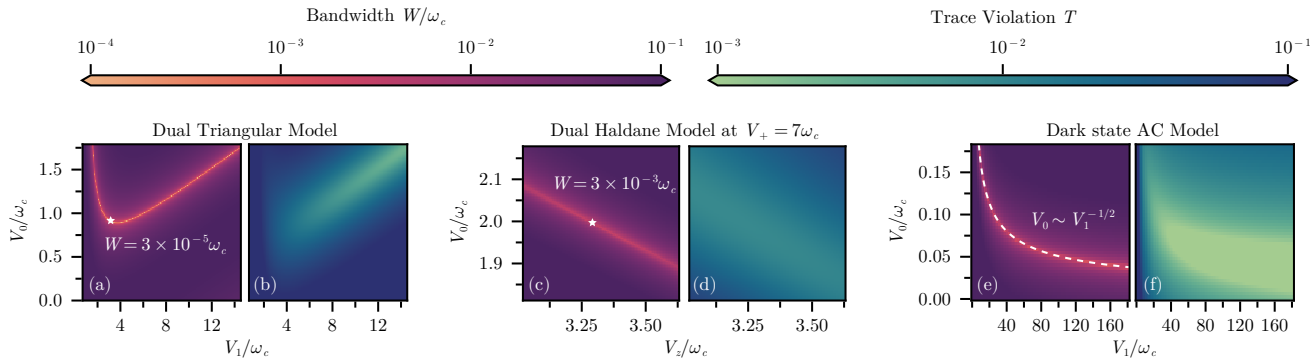


FIG. 4. Bandwidth (a,c,e) and trace violation (b,d,f). In all three cases clear codimension-1 manifolds of extremely narrow bands are visible. The minimal bandwidths of the dual triangular and Haldane models are indicated by ⋆, and match the expectation for the 1-flat manifold given their C_6 π-flux respectively 2π-flux symmetries. In contrast, the trace violation achieves its minimum close to the 1-flat manifold in all cases, but grows slowly in the surrounding region (it remains far below the value $T = 2$ characteristic of the 1st Landau level).

Haldane model (10). In Fig. 4 we take two-dimensional parameter cuts, in the latter case fixing $V_+ = 7\omega_c$, and calculate their bandwidths and the trace violations (20). In sharp agreement with our considerations, we see a parameter region of size $\sim \omega_c$ where the trace violation is comparable to 10^{-2} or less in both models. Intersections of the centers of these parameter regions are clear codimension-1 flat manifolds, with minimal bandwidths of $3.4\times10^{-5}\omega_c$ in the dual triangular case or $3.5\times10^{-3}\omega_c$ in the dual Haldane case. This matches the expectation for 1-flat bands from Table I. While it may be tempting to believe that these ultra-narrow bands arise because the models are similarly close to having an AC form, that belief is not true. Consider for example the parameter point $(V_z, V_+, V_0) = (3.06, 7.06, 2.09)\omega_c$ of the dual Haldane model which lies along the 1-flat manifold. We plot various characteristics of this parameter point in Fig. 5. The band is essentially ideal, as can be measured by the trace violation of 0.009, and the overlap between the true and ideal wavefunction predicted by $\hat{H}$ is $|\langle\mathbf{k}|\bar{\chi}\chi_{0\mathbf{k}}|\mathbf{k}\rangle| = 0.995 \pm 0.002$ across the Brillouin zone, with the quoted variation being the standard deviation. Surprisingly we note that directly optimizing the average square overlap between the true lowest band and the ideal wavefunction via gradient descent, similar to [46], yields an average overlap only 10^{-4} better than the ground state of $\tilde{H}$. The bandwidth is $6\times10^{-3}\omega_c$, and the band gap is $0.7\omega_c$ in agreement with the 1-flat condition for models with C_6 2π-flux symmetry. In contrast to the uniform Landau level, there is no expectation that the Berry curvature is uniform, or that the excited bands are flat. The former fluctuates $-\ell_B^2(1\pm0.2)$, and the bandwidth of the first excited band is $0.7\omega_c$. To understand the proximity to the AC limit, we compute the potential difference between the AC and adiabatic Hamiltonian for the ground

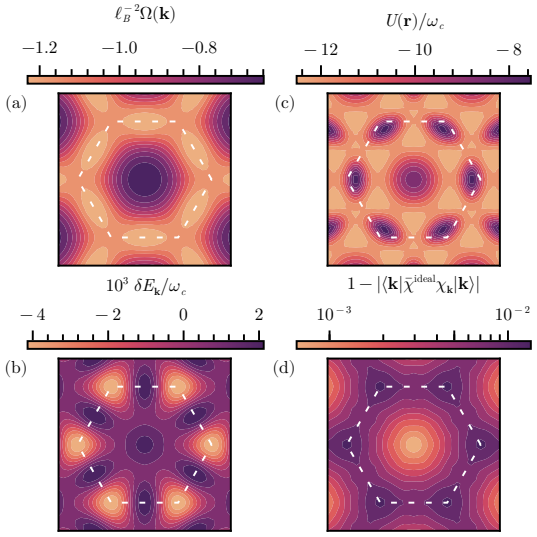


FIG. 5. Characteristics of the dual Haldane model at parameters $(V_z, V_+, V_0) = (3.06, 7.06, 2.09)\omega_c$. The Berry curvature (a) fluctuates $\Omega(\mathbf{k}) = -\ell_B^2(1\pm0.2)$. By contrast the dispersion (b), which is measured against the average of the lowest band $E = -11.25\omega_c$, is nearly flat. Further, the overlap (d) between the true wavefunction, as computed by (27), and the optimal ideal wavefunction solving (29) is nearly unity across the entire Brillouin zone. The residual potential deviation from the adiabatic AC limit (c) fluctuates in the range $U(\mathbf{r}) \in [-12.5, -7.5]\omega_c$.

state texture at this parameter point

$$U(\mathbf{r}) = \frac{B_{\rm texture}(\mathbf{r}) + D(\mathbf{r})}{2M} + \bar{n}_\alpha V_\beta^\alpha n^\beta\,. \qquad (33)$$

The root mean square variation of $U(\mathbf{r})$ is $1.2\omega_c$ across the unit cell, with a range of $5\omega_c$. Naively, it is immensely

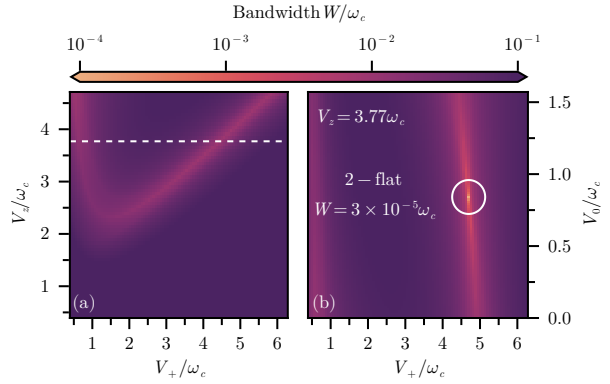


FIG. 6. Bandwidth of dual square model with potential (12) along parameter cuts with (a) $V_0 = 0$ and (b) $V_z = 3.77\omega_c$. A clear 1-flat manifold of codimension-1 can be seen with bandwidth comparable to $10^{-2}\omega_c$, while the circled point indicates the presence of the 2-flat manifold with bandwidth $3 \times 10^{-5}\omega_c$

surprising, and highlights the power of our analysis, that an AC deviation comparable to the single particle gap destroys neither ideality nor the flat band.

In principle the bandwidth of the dual Haldane model could be reduced even more, by tuning to the 2-flat condition. This would be achieved by adding a further scalar potential to the model (10), with wavevectors that lie on the second reciprocal space shell Λ_2^*. Instead, we illustrate the 2-flat condition for the dual square lattice.

A. 2-Flat bands in the dual square model

Using the three tuning parameters $V_{0,+,z}$ of the dual square model (12) we find it possible to reach not just 1-flatness, but also the 2-flat manifold of parameters. Because it is the simplest parameter regime, consider first $V_0 = 0$. In Fig. 6 we see the clear presence of a 1-flat manifold, with minimal bandwidth $7 \times 10^{-3}\omega_c$. This is in fair agreement with the second form factor $|I_{\mathbf{G}\in\Lambda_2^*}| = 2 \times 10^{-3}$. It is worth emphasizing that the 1-flat condition is less restrictive in square lattices than it is in triangular lattices, as the second shell is closer to the first shell in the former case, see the illustration in Table I. To achieve a bandwidth comparable with the 1-flat triangular model, we instead need to reach the 2-flat manifold. To do this we turn on the additional scalar lattice V_0. Remarkably, we find that for a range of parameter cuts a 2-flat manifold is apparent. For example taking $V_z = 3.77\omega_c$, which is illustrated in Fig. 6, a codimension-2 manifold (in this case a point) of bands with width $3 \times 10^{-5}\omega_c$ appears. This is slightly larger than predicted by the 2-flat condition, which we suspect is due to the non-ideal perturbations.

B. Dark OFL

From the dual Haldane example it is clear that 1-flat bands can be achieved by adding a suitably tuned scalar lattice even when the adiabatic Hamiltonian is far from the AC limit. In that example the band is also nearly ideal, because, as shown in Sec. III, the deviation from the AC limit—although comparable to ω_c—only weakly perturbs ideality. We stress, however, that this is a consequence of proximity to an AC Hamiltonian rather than of flatness itself: in general, flatness and ideality are independent properties of a band, and a flat band need not be ideal. Moreover, in that example neither flatness nor ideality is exact. We will now introduce an OFL that is an *exact* AC Hamiltonian in the adiabatic limit — a qualitatively stronger result. While the AC Hamiltonian has been developed as a theoretical ideal [32, 34], realizations in condensed matter systems achieve this structure only approximately. The dark-state OFL constructed below achieves it exactly, yielding perfectly flat and exactly ideal Chern bands as an analytical statement. This provides a physical platform in which their idealized limit is realized precisely, and against which the quality of AC approximations in moiré systems can be calibrated. Nevertheless adding a tunable scalar lattice still permits a huge further decrease in the bandwidth beyond the adiabatic limit. As was shown in [45], OFLs can be constructed also for so-called "dark" lattices, for which the optically dressed state is exactly decoupled from the optical fields, and lies at the lowest energy with all other "bright" levels being energetically repulsed. (See Refs. [35, 36] for reviews of previous research into dark-state systems with synthetic gauge fields, and Ref. [47] for other dark state topological lattices.) Dark optical lattices can be understood straightforwardly from their dual tight-binding models. Including both N ground states α and $\tilde{N}$ excited states $\tilde{\alpha}$, a dark lattice arises when there are no potential couplings connecting ground states $V_\beta^\alpha(\mathbf{r}) = 0$, and the number of coupled ground states exceeds the number of excited states $N > \tilde{N}$. Then the off-diagonal part of the potential $V_\beta^{\tilde{\alpha}}(\mathbf{r})$ must have a kernel of dimension $N - \tilde{N} > 0$, which describes textures with exactly zero potential energy, the "dark" states. When the dark-state texture has net flux per unit cell, these are dark OFLs. It is well known [48] that flat bands of tight-binding models cannot be energetically isolated and possess nonzero Chern number: coming from a tight-binding model in reciprocal space, the real-space texture in dark OFLs must be degenerate with a different bright texture at least at one point in the unit cell. This makes the adiabatic limit more subtle as the gap must be due to the zero-point motion of the atom. As noted in [45] for different dark OFLs, the bright-state gap generically vanishes quadratically around the gapless point. If V_1 is the characteristic size of the potential, the bright state zero-point energy is $\propto \sqrt{MV_1}$. As $V_1 \to \infty$ the model will project perfectly onto the adiabatic subspace of dark states, and be governed by the adiabatic Hamiltonian (4) with geometric potential

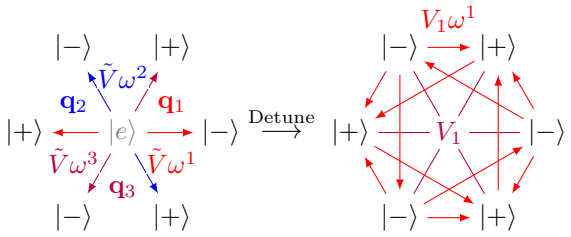


FIG. 7. Detuning the excited state by Δ_e in a three-state dark OFL results in a two-state OFL. Two original couplings v_1, v_2 with momenta transfers $\mathbf{q}_1$ and $\mathbf{q}_2$ result in a new coupling with amplitude $v_1\bar{v}_2/\Delta_e$ and momentum transfer $\mathbf{q}_1 - \mathbf{q}_2$.

contribution $D(\mathbf{r})/2M$. For most dark OFLs this potential is significant as $D(\mathbf{r}) \geq |B_{\text{texture}}(\mathbf{r})|$, hence $D(\mathbf{r})/2M$ is generically a fluctuating potential comparable to the natural cyclotron energy of the problem. This means that even as $V_1 \to \infty$ a generic dark OFL will *not* lead to a flat Chern band, even in the absence of diabatic corrections, which decay with the reciprocal zero-point energy $\propto 1/\sqrt{V_1}$. An exactly flat band in this limit requires the special, non-generic condition that $D(\mathbf{r}) + B_{\text{texture}}(\mathbf{r})$ is constant, such that the adiabatic Hamiltonian is of exact AC form. Below we present a dark OFL for which this exceptional condition is met. As our earlier considerations show, while precluding exact flat bands, perturbations of this magnitude to the AC limit largely preserve ideality. This matches the observations that dark state OFLs are very close to ideality, which was noted in [47] and [45].

We consider a novel dark OFL dual to the tight-binding model in [49]. This model corresponds to a dark lattice with uniform flux in reciprocal space. Let Δ_e,$\tilde{V}$ be potential parameters, and $|e\rangle$ an excited state above the two ground states $|\alpha = \pm\rangle$. In particular we define the optical potential

$$\hat{V}(\mathbf{r}) = -\Delta_e |e\rangle\langle e| + \tilde{V} \sum_{a=1,\alpha=\pm}^{3} \mathrm{e}^{-\mathrm{i}\alpha\mathbf{q}_a\cdot\mathbf{r} - \frac{2\mathrm{i}a\pi}{3}} |\alpha\rangle\langle e| + \text{h.c.} \tag{34}$$

The (unnormalized) bright state $|s\rangle$, with coefficients $\langle\alpha|s\rangle \equiv s^\alpha(\mathbf{r}) = \sum_a \mathrm{e}^{-\mathrm{i}\alpha\mathbf{q}_a\cdot\mathbf{r} - 2\pi\mathrm{i}a/3}$ is orthogonal to the (unnormalized) dark state $|d\rangle$ with $\langle\alpha|d\rangle \equiv d^\alpha(\mathbf{r}) = \alpha\sum_a \mathrm{e}^{-\mathrm{i}\alpha\mathbf{q}_a\cdot\mathbf{r} + 2\pi\mathrm{i}a/3}$, which is an exact zero mode of (34). When $|\Delta_e| \gg |\tilde{V}|$ the excited state is far detuned and can be eliminated using perturbation theory, to yield the effective potential $V_\beta^\alpha(\mathbf{r}) = V_1 s^\alpha(\mathbf{r})\bar{s}_\beta(\mathbf{r})$, where $V_1 = \tilde{V}^2/\Delta_e$, as illustrated in Fig. 7. The precise model we consider adds to this dark OFL a scalar lattice of strength V_0, to give a total potential

$$(V^\Lambda)_\beta^\alpha(\mathbf{r}) = V_1 s^\alpha \bar{s}_\beta + \delta_\beta^\alpha V_0 \sum_a \left[\mathrm{e}^{\mathrm{i}\mathbf{G}_a\cdot\mathbf{r}} + \mathrm{e}^{-\mathrm{i}\mathbf{G}_a\cdot\mathbf{r}}\right], \tag{35}$$

where $\mathbf{G}_2 = \mathbf{q}_2 - \mathbf{q}_1$ etc. as before. The scalar lattice does not alter the dark-state texture $d^\alpha(\mathbf{r})$, but it does contribute a nonzero, spatially varying potential to the adiabatic Hamiltonian. We therefore first consider $V_0 = 0$. For $V_0 = 0$, due to the vanishing potential of the ground state texture, the difference between the adiabatic Hamiltonian (4) and the AC Hamiltonian (13) is $U(\mathbf{r}) = \frac{1}{2M}[D(\mathbf{r}) + B_{\text{texture}}(\mathbf{r})]$. Remarkably, this is a constant, so this model possesses an exact flat band in the adiabatic limit. To see this choose a coordinate system so that $q_{ax} + \mathrm{i}q_{ay} = |\mathbf{q}|\mathrm{e}^{2\pi\mathrm{i}a/3}$, from which it follows that $(\partial_x + \mathrm{i}\partial_y)d^\alpha = -\mathrm{i}|\mathbf{q}|\sum_a \mathrm{e}^{-\mathrm{i}\alpha\mathbf{q}_a\cdot\mathbf{r} + 4\pi\mathrm{i}a/3} = -\mathrm{i}|\mathbf{q}|s^\alpha$, and since $\langle -|s\rangle = \langle d|+\rangle, \langle +|s\rangle = -\langle d|-\rangle$ their normalizations agree $|d|^2 = |s|^2$. We will also need the orthogonal projector $Q_\beta^\alpha = \delta_\beta^\alpha - \frac{d^\alpha \bar{d}_\beta}{|d|^2}$, which clearly satisfies $Q_\beta^\alpha d^\beta = \bar{d}_\alpha Q_\beta^\alpha = 0$ and $s^\alpha = Q_\beta^\alpha s^\beta$. As such

$$U(\mathbf{r}) = \frac{1}{2M}\left[(\partial_x - \mathrm{i}\partial_y)\frac{\bar{d}_\alpha}{|d|}\right] Q_\beta^\alpha \left[(\partial_x - \mathrm{i}\partial_y)\frac{d^\beta}{|d|}\right] \tag{36}$$

$$= \frac{1}{2M|d|^2}\left[(\partial_x - \mathrm{i}\partial_y)\bar{d}_\alpha\right] Q_\beta^\alpha \left[(\partial_x - \mathrm{i}\partial_y)d^\beta\right] \tag{37}$$

$$= \frac{\mathbf{q}^2|s|^2}{2M|d|^2} \tag{38}$$

$$= \frac{\mathbf{q}^2}{2M}. \tag{39}$$

Hence in the adiabatic limit $V_1 \to \infty$ with $V_0 = 0$ there must be an exactly flat band with energy $\mathbf{q}^2/2M$. A nonzero V_0 adds the potential $V_0\sum_a 2\cos(\mathbf{G}_a\cdot\mathbf{r})$ to $U(\mathbf{r})$, and so breaks the exact AC form; as we show below, a small V_0 is nevertheless useful at finite V_1 to compensate for diabatic corrections. We emphasize that this is an exact analytical result: the dark-state texture of this OFL satisfies $D(\mathbf{r}) + B_{\text{texture}}(\mathbf{r}) = \text{const}$, which is precisely the condition for the adiabatic Hamiltonian to reduce to AC form. In Fig. 4 we show the model's phase diagram. Even at $V_0 = 0, V_1 = 180\omega_c$ the bandwidth is $5\times10^{-2}\omega_c$, which is far larger than that of the dual Haldane model. By contrast, adding a tiny scalar potential of magnitude $V_0 \sim 0.5\omega_c^{3/2}/\sqrt{V_1}$ we find a 1-flat manifold whose bandwidth at $(V_1, V_0) = (181, 0.038)\omega_c$ is $1\times10^{-3}\omega_c$, while the trace violation achieves a minimum value of 2×10^{-6} at $(V_1, V_0) = (50, 0.048)\omega_c$. The strength of the requisite scalar potential follows from the fact that it must cancel diabatic corrections, while the quoted coefficient is found by an empirical least squares fit to the 1-flat manifold. This model reveals that reaching the flat bands is more subtle than simply canceling the potential deviation $U(\mathbf{r})$ from the AC limit – the diabatic corrections shift the location of the 1-flat manifold, even as they do not destroy it. Notably though, a tunable scalar lattice is sufficient to reach the 1-flat manifold, even though there cannot be any direct cancellation between it and the diabatic perturbation to the Hamiltonian. Furthermore, since the deviation from the AC limit is much smaller in magnitude than the other examples, the band is much closer to ideality.

Beyond the cold-atom setting, the exact AC equivalence found here suggests a concrete design goal for multilayer TMD heterostructures. Rather than only approximating the AC form, as in twisted bilayers, one can ask which tun-

neling structure would precisely realize it. An intriguing observation to this effect is that the dark OFL potential of Eq. (34) naturally occurs in the interlayer potential of the favored moiré scale domains of helically twisted (homo or hetero)trilayer transition metal dichalcogenide heterostructures. In particular, we identify the state $|e\rangle$ with the central layer and the states $|\alpha = \pm\rangle$ with the top and bottom layer, which as explored in [50] for other reasons form moiré-scale domains wherein the outer layers are displaced in-plane in opposite directions from the central layers by $\Delta x = \pm a_m/\sqrt{3}$, where a_m is the moiré lattice constant. The required tunneling structure and phases that give rise to an interlayer potential of the form in Eq. (34) emerge without fine tuning in this setting, and the ratio of kinetic to potential energy can, as usual, be tuned by varying the twist angle. In contrast to the dark OFL potential there may be further important interlayer potential contributions, whose relative magnitude would depend on the exact material platform. We leave a detailed analysis for further work, beyond noting that the layer offset Δ_e in Eq. (34) would be especially natural in the heterotrilayer context, and that this proposed platform provides a genuinely ideal Chern band based in the adiabatic limit of small twist angle.

V. STRONGLY CORRELATED PHASES

Our considerations have yielded a zoo of nearly flat bands, with which one can hope to reach the strongly correlated regime. We focus on bosonic atoms, for which cold atom platforms offer the greatest differences from solid state systems[51]. Also, in the adiabatic limit the flat bands are perfectly spin polarized at each point in real space, along the local spinor $n^\alpha(\mathbf{r})$. For fermionic isotopes, contact (s-wave) interactions then vanish by Pauli exclusion. Away from this limit, the non-adiabatic motion of the atoms admixes the other internal state, leading to residual, but much weaker, interparticle interactions between fermions[41]. Ignoring the species dependence of the scattering length a_s, the effective two-dimensional interaction takes the form

$$V^{\rm int}(\mathbf{r}_1 - \mathbf{r}_2) = \frac{\tilde{g}}{M}\delta^{(2)}(\mathbf{r}_1 - \mathbf{r}_2) \tag{40}$$

where a vertical confinement with oscillator length a_z yields $\tilde{g} = \sqrt{8\pi}a_s/a_z$. We consider N_B bosons occupying a band of N_Φ states, having filling factor $\nu = N_B/N_\Phi$. The natural energy scale for the interaction in the LLL is the zeroth Haldane pseudopotential strength $v_0 = \tilde{g}\omega_c/4\pi$, the size of which sets the typical many body gap for quantum Hall phases. At the coarsest level, the competition between a Bose superfluid and a strongly correlated phase will fall to the latter's favor when v_0 exceeds the bandwidth. For a 1-flat band, given the proximity to ideality, an optimistic estimate is therefore that strong correlations can be reached when $\tilde{g}$ is larger than the characteristic

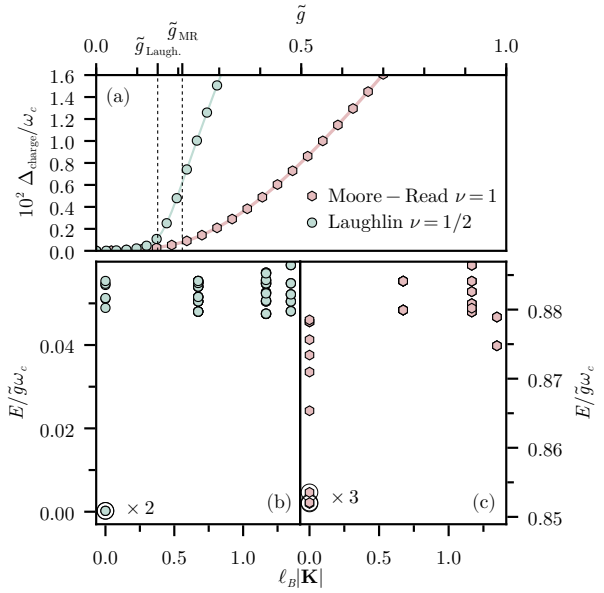


FIG. 8. Many-body characteristics of the dual Haldane model at parameters $(V_z, V_+, V_0) = (3.06, 7.06, 2.09)\omega_c$ at fillings $\nu = 1/2, 1$. The charge gap $\Delta_{\rm charge}$ (a) computed with $(N_B, N_\phi) = (8, 16), (12, 12)$. The exact diagonalization spectra at filling $\nu = 1/2$ (b) and $\nu = 1$ (c) absent dispersion computed with $(N_B, N_\phi) = (8, 16), (16, 16)$ respectively. The nearly degenerate states are circled and their multiplicity noted. The many body crystal momentum $\mathbf{K}$ is measured from the origin of the Brillouin zone.

value

$$\tilde{g}_{\rm char} \sim 4\pi |I_{\mathbf{G}\in\Lambda_2^\star}| = \begin{cases} 0.05 & C_6\ 2\pi\text{-flux} \\ 0.0002 & C_6\ \ \pi\text{-flux} \\ 0.5 & C_4\ 2\pi\text{-flux} \\ 0.02 & C_4\ \ \pi\text{-flux} \end{cases} \tag{41}$$

Experimentally, interactions as strong as $\tilde{g} \sim 0.6$ have been realized[52], making all options bar the C_4 2π-flux models appealing experimental candidates. To reach $\tilde{g} \sim 0.26$ in ^{87}Rb[53], where the scattering length is $a_s \simeq 100 a_{\rm Bohr}$, the vertical trap frequency needs to be $\omega = \tilde{g}^2/8\pi M a_s^2 = 2\pi \times 10\,{\rm kHz}$.

For any N_B-particle wavefunction in the LLL $\psi^{\rm LLL}(\mathbf{r}_1 \ldots \mathbf{r}_{N_B})$ there is a natural ideal analogue

$$\psi^{\rm ideal}(\mathbf{r}_1\alpha_1 \cdots) \propto \psi^{\rm LLL}(\mathbf{r}_1 \cdots) \prod_{i=1}^{N_B} \chi^{\alpha_i}(\mathbf{r}_i)\,. \tag{42}$$

Ignoring the spinor direction, for model states arising as correlation functions of conformal field theories[5, 54], or from the Coulomb gas analogy[55], this can be thought of as a modification to the neutralizing background 'charge' in those descriptions to be proportional to the effective magnetic field $\ell_B^{-2} - \nabla^2\phi$. Spinor-independent expectation

values $\langle\cdot\rangle^{\text{ideal}}$ from ψ^{ideal} are simply Gibbs reweightings of those $\langle\cdot\rangle^{\text{LLL}}$ from ψ^{LLL}[56]

$$\langle f(\mathbf{r}_1\cdots\mathbf{r}_{N_B})\rangle^{\text{ideal}} = \frac{\left\langle e^{2\sum_i\phi(\mathbf{r}_i)} f(\mathbf{r}_1\cdots\mathbf{r}_{N_B})\right\rangle^{\text{LLL}}}{\left\langle e^{2\sum_i\phi(\mathbf{r}_i)}\right\rangle^{\text{LLL}}}. \quad (43)$$

If f is such an observable which is positive definite and for which $\langle f\rangle^{\text{LLL}} = 0$ it follows immediately that $\langle f\rangle^{\text{ideal}} = 0$ for any non-singular ϕ. At filling $\nu = 1/2$, the Laughlin wavefunction [55] of bosons $\psi^{\text{LLL}}_{\text{Laugh.}} = \prod_{i<j}(z_i - z_j)^2 e^{-\sum_i |z_i|^2/4\ell_B^2}$ has vanishing interaction energy. Hence, irrespective of ϕ, the interaction energy will vanish in an ideal band, ensuring that the ideal analogue is a ground state. At filling $\nu = 1$, the ground state of the bosonic LLL is known to be the Moore-Read Pfaffian[4], possessing model wavefunction $\psi^{\text{LLL}}_{\text{MR}} = \text{Pf}(\frac{1}{z_i - z_j})\prod_{i<j}(z_i - z_j)e^{-\sum_i |z_i|^2/4\ell_B^2}$. By contrast to the Laughlin state, the interaction energy is non-vanishing due to the finite probability of coincident particles. Using a 'mean-field' approximation to describe the change in the correlation functions due to $\phi \neq 0$[57], the ground state energy takes the form

$$E^{\text{ideal}}_{\text{gs}} \simeq \frac{2\pi\ell_B^2 \int d\mathbf{r}\, e^{4\phi}}{\left[\int d\mathbf{r}\, e^{2\phi}\right]^2} E^{\text{LLL}}_{\text{gs}} = \frac{\langle e^{4\phi}\rangle_{\text{uc}}}{\langle e^{2\phi}\rangle^2_{\text{uc}}} E^{\text{LLL}}_{\text{gs}}. \quad (44)$$

At intermediate fillings $1/2 < \nu \lesssim 6$, the quantum Hall states in the bosonic LLL compete with other states, notably charge-density-ordered stripe phases[1]. Depending on whether their period is commensurate/incommensurate with Λ_{pot}, these competing charge-density-ordered states could be favored/disfavored by the lattice-scale modulations. Thus we expect the stability of the Moore-Read state to be sensitive to ϕ, and must be checked on a case-by-case basis.

To understand how these considerations manifest empirically, we consider the dual Haldane model at the generic 1-flat parameter point $(V_z, V_+, V_0) = (3.06, 7.06, 2.09)\omega_c$ as in IV. We perform exact diagonalization on the lowest band of the model on C_6 symmetric super-cells containing $N_\phi = 12, 16$ unit cells. Consider first the strong interaction limit, where the bandwidth is artificially set to 0. Consistent with the proximity to ideality we find 2-fold degenerate ground states at filling $\nu = 1/2$ ($N_B = 6, 8$) with near-vanishing energy per particle $E/N_B = (4.8 \pm 0.2) \times 10^{-3}\tilde{g}\omega_c$, see Fig. 8. The uncertainty quoted is the energy difference between the two lattice sizes. At filling $\nu = 1$ ($N_B = 12, 16$) we instead find three nearly degenerate ground states. This is consistent with the Moore-Read state. The correlation length is sufficiently large that the ground state degeneracy is not clearly developed in non C_6 symmetric super-cell geometries. This is likely exacerbated by the aforementioned competing crystalline stripe phase at intermediate fillings. The $\nu = 1$ Moore-Read state in the Landau level has ground state energy $E^{\text{LLL}}_{\text{gs}} \simeq 4.8\times10^{-2}\tilde{g}\omega_c N_B$[1], whereas it takes the value $E^{\text{ideal}}_{\text{gs}} = 5.3 \times 10^{-2}\tilde{g}\omega_c N_B = 1.1 E^{\text{LLL}}_{\text{gs}}$ in the ideal band. From single-particle numerics we find $\langle e^{4\phi}\rangle_{\text{uc}} / \langle e^{2\phi}\rangle^2_{\text{uc}} = 1.1$, so the ground state energy of the Moore-Read state perfectly matches our ideal estimate (44).

The many-body gaps are comparable to those in the LLL. The neutral gap Δ_{neutral} is computed as the difference in energy between the first excited state and the lowest of the degenerate ground states, while the charge gap Δ_{charge} is obtained from the ground state energies with $N_B, N_B \pm 1$ particles as:

$$\frac{\Delta_{\text{charge}}}{N_B} = \frac{E_{\text{gs}}(N_B+1)}{N_B+1} + \frac{E_{\text{gs}}(N_B-1)}{N_B-1} - \frac{2E_{\text{gs}}(N_B)}{N_B} \quad (45)$$

At half filling $\Delta^{\nu=1/2}_{\text{neutral}} \simeq (4.9 \pm 0.1) \times 10^{-2}\tilde{g}\omega_c$ and $\Delta^{\nu=1/2}_{\text{charge}} = (7.5\pm0.6)\times10^{-2}\tilde{g}\omega_c$ which are indistinguishable from those in the LLL with the same particle number. For a typical experimental value of the cyclotron frequency $\omega_c = 2\pi \times 1\,\text{kHz}$ and $\tilde{g} = 0.6$, the resulting charge gap is therefore $2\pi \times (45 \pm 4)\,\text{Hz}$. In Fig. 8 we furthermore see that the neutral excitations have lowest energy near $\ell_B|\mathbf{K}| \sim 1$, which is consistent with the typical location of the magneto-roton minimum[58], indicating that dynamics in this phase are very similar to that in the LLL. At unit filling we find $\Delta^{\nu=1}_{\text{neutral}} = (1.3 \pm 0.1) \times 10^{-2}\tilde{g}\omega_c$ which is smaller than the neutral LLL gap of $1.8 \times 10^{-2}\tilde{g}\omega_c$ we compute for $N_\phi = 12$. We compute the charge gap $\Delta^{\nu=1}_{\text{charge}} = 2.5 \times 10^{-2}\tilde{g}\omega_c$ at $N_\phi = 12$, which is also smaller than in the LLL where it takes the value $4.5 \times 10^{-2}\tilde{g}\omega_c$. While smaller than the LLL gaps, they remain large in absolute terms. Furthermore Δ_{neutral} increases between $N_B = 12 \to 16$, giving us confidence that the Moore-Read state survives to the thermodynamic limit. To estimate the necessary $\tilde{g}$ to reach the phase transition from the Bose superfluid at $\tilde{g} = 0$, we compute the charge gap as a function of $\tilde{g}$, as shown in Fig. 8. In the Bose superfluid the charge gap vanishes, while it increases linearly as a function of $\tilde{g}$ in the strongly correlated phase. Finite size effects smear the transition, though for the Laughlin state at $\nu = 1/2$ (computed using $N_B = 8$) there is a very clear transition around $\tilde{g}_{\text{Laugh.}} \simeq 0.15$, where the slope $d\Delta_{\text{charge}}/d\tilde{g}$ reaches half the asymptotic value, which we will use as our criterion to characterize the transition point in other cases. At $\nu = 1$ ($N_B = 12$) the slope $d\Delta^{\nu=1}_{\text{charge}}/d\tilde{g}$ reaches half its asymptotic value at $\tilde{g}_{\text{MR}} \simeq 0.2$, but we caution that the transition point of the Moore-Read state is ill-resolved due to the larger correlation length at accessible system sizes. In Appendix A we show further exact diagonalization results supporting the existence of the Laughlin and more broadly Jain states at $\nu = 1/2, 2/3, 3/4$ in the dual Haldane, triangular, and square models, their charge gap across the superfluid to Laughlin state transition, and further comparisons with the LLL ED spectra. For the dual triangular (square) models at a 1-flat parameter point with bandwidth $W^{1-\text{flat}}_{\triangle} = 3 \times 10^{-5}\omega_c$ ($W^{1-\text{flat}}_{\square} = 10^{-2}\omega_c$) we find a transition with $\tilde{g}^{1-\text{flat}}_{\triangle} = 3 \times 10^{-4}$ ($\tilde{g}^{1-\text{flat}}_{\square} = 0.2$), in good agreement with (41). Since all of these models

are essentially ideal, it is reasonable that the transition point is simply proportional to the bandwidth, which is supported by the fact that the aforementioned 2-flat parameter point in the dual square model has bandwidth $W_{\square}^{2-\text{flat}} = 3 \times 10^{-5}\omega_c$, and transitions to a Laughlin state at $\tilde{g}_{\square}^{2-\text{flat}} = 5 \times 10^{-4}$. Comparing the 1- and 2-flat dual square models, which differ in bandwidth by three orders of magnitude but are otherwise the same model, isolates the role of the bandwidth itself in controlling the onset of the strongly correlated phase. While the ground state degeneracy is less clearly developed in $\hat{V}^{\triangle}$ at $\nu = 1$, we do find appealing evidence of the Moore-Read state's existence. With $N_B = 12$ bosons, there are 3 putative ground states separated from any excited states by a neutral gap $2 \times 10^{-2}\tilde{g}\omega_c$, and furthermore, the low-energy spectrum near-perfectly matches the lowest 50 eigenvalues in the LLL in every momentum sector, differing on average only 1.5% (after subtracting the ground state energy).

VI. DISCUSSION AND CONCLUSION

We have shown that, while generically optical flux lattice potentials do not permit direct access to the exact AC Hamiltonian, they still support nearly flat and ideal bands through the addition of a suitable scalar potential.

Reaching the exact AC point would require control over generic scalar potentials, and the addition of counterdiabatic terms, which are typically not perturbations one can experimentally access. However, the size of these perturbations is comparable to ω_c in the regions of interest, and so by the analysis of the paper, we see that the nearly ideal region should broadly be present in the accessible parameter space.

By tuning one potential parameter for lattices with C_6 2π-flux and $C_{4,6}$ π-flux symmetries, one can reach 1-flat bands, for which the interaction strength $\tilde{g}$ can readily be made big enough in experiment, to reach the Laughlin, Jain sequence, and Moore-Read states. Although a 1-flat band in many cases already suffices for this purpose, the value of tuning to still narrower bands is mainly conceptual.

In sharp contrast to this is the dark-state OFL of Sec. IV B, whose adiabatic Hamiltonian is *exactly* of Aharonov-Casher form. This is, to our knowledge, the first exact physical realization of the AC structure with nonzero Chern number, in any platform. The AC Hamiltonian has been established as a theoretical ideal [32, 34]. Due to the flexibility of this approach, the principal challenge remains to realize a suitable host OFL potential. In alkali-metal gases this is complicated by the fact that the dominant contributions to the polarizability typically arise from the $D_{1,2}$ lines, with opposite vector polarizability. To craft a state-dependent lattice potential, the laser frequency must be suitably close to these transitions, which necessarily begets photon scattering. However, for heavy atoms like Rb or Cs, this photon scattering need not be prohibitive for the lifetime. In Appendix B we give examples of experimental setups that can realize the dual Haldane and square models. The photon scattering rate in these setups is of order $1 - 6 \times 10^{-4}\omega_c$. For ^{87}Rb, a wavelength of $\lambda = 810\,\text{nm}$ yields a photon scattering rate around $0.8 - 1.6\,\text{s}^{-1}$. In the case of ^{133}Cs, with red detuned beams at wavelength $\lambda = 950\,\text{nm}$, it can be as low as $0.1\,\text{s}^{-1}$. The photon scattering can be further reduced using other atomic species (including Dy, Er, or Ti) where state-dependent Raman coupling can be achieved with far-detuned light. Instead of using far-detuned light, it is interesting to note that, absent many-body effects, photon scattering from (near) resonant levels can in principle be reduced arbitrarily in dark lattice setups by increasing the laser power, though to our knowledge, experimentally achieved dark-lattice lifetimes remain small[59]. To shape higher-shell Fourier components of the lattice, one particularly interesting technique, is the realization of optical potentials using programmable holographic techniques[60]. Beyond photon scattering, we caution that magnetic field noise will likely pose an important experimental obstacle, as it contributes a non-uniform perturbation to the system. Reaching a target filling additionally requires controlling the particle density, which can be tuned via the depth and shape of the confining potential; incompressible states are comparatively easy to target, since the many-body gap locks the density to its quantized value over a finite range of chemical potential, with a Mott-insulator gap in a superlattice offering one likely route to loading a low-entropy state at fixed density before evolving into the topological phase. Once prepared, the topological character of these phases can be probed in several complementary ways, including Hall drift measurements and probes of edge modes and bulk fractionalized quasiparticles. In the near term, the most direct route is likely to be the measurement of multi-particle correlation functions, which characterize the many-body wavefunction itself[61]. This approach has recently been used to identify a lattice Moore-Read state, via a suppression of short-range three-body density correlations together with a Hall drift measurement[62]. Irrespective of atomic species, we have provided a general approach by which to realize flat ideal Chern bands and robust fractional quantum Hall states. The ability to precisely tune band geometry will enable systematic studies of the transition into exotic topologically ordered phases, including the non-Abelian states sought for fault-tolerant quantum computation. Furthermore, this approach strengthens the connection between cold atoms and moiré materials, promising a new, highly controllable platform to probe the fundamental principles of strongly correlated systems and test theoretical models of ideal band structures in a clean, controllable, and, well-characterized experimental environment. While the two-state OFLs studied here, built from the Aharonov-Casher form, are restricted to bands of unit Chern number, reciprocal-space lattice constructions are known to realize bands of higher Chern number[15]; we anticipate that a similar scalar-potential tuning could flatten such bands, though we have not explored this here.

Note added: After completion of this work we learned that the authors of Ref. [45] have now found a square version of a dark OFL which, using an analysis mirroring (36-39), one can show shares the property of (34) that it has an exact flat band in the adiabatic limit. For finite lattice depth, it is similarly amenable to band-flattening using scalar potentials on $\Lambda^*_{1,2,...}$ momentum shells.

VII. ACKNOWLEDGMENTS

We thank Patrick Ledwith, Tomohiro Soejima, Monika Aidelsburger, Dan Parker, Ashvin Vishwanath, Alexander Douglas, and Clemens Kuhlenkamp for helpful discussions, and Jean Dalibard for helpful discussions and for sharing an updated version of Ref. [45]. This work was supported by a Simons Investigator Award (Grant No. 511029) and the Engineering and Physical Sciences Research Council [grant numbers EP/V062654/1 and EP/Y01510X/1]. O.E.S. was funded by NSF DMR-2220703.

[1] N. R. Cooper, Rapidly rotating atomic gases, Advances in Physics **57**, 539 (2008).
[2] A. L. Fetter, Rotating trapped Bose-Einstein condensates, Rev. Mod. Phys. **81**, 647 (2009).
[3] N. K. Wilkin, J. M. F. Gunn, and R. A. Smith, Do attractive bosons condense?, Phys. Rev. Lett. **80**, 2265 (1998).
[4] N. R. Cooper, N. K. Wilkin, and J. M. F. Gunn, Quantum phases of vortices in rotating Bose-Einstein condensates, Phys. Rev. Lett. **87**, 120405 (2001).
[5] G. Moore and N. Read, Nonabelions in the fractional quantum Hall-effect, Nuclear Physics B **360**, 362 (1991).
[6] N. Regnault and T. Jolicoeur, Quantum Hall fractions in rotating Bose-Einstein condensates, Phys. Rev. Lett. **91**, 030402 (2003).
[7] N. Read and E. H. Rezayi, Beyond paired quantum Hall states: Parafermions and incompressible states in the first excited Landau level, Phys. Rev. B **59**, 8084 (1999).
[8] E. H. Rezayi, N. Read, and N. R. Cooper, Incompressible liquid state of rapidly rotating bosons at filling factor 3/2, Phys. Rev. Lett. **95**, 160404 (2005).
[9] P. Lunt, P. Hill, J. Reiter, P. M. Preiss, M. Gałka, and S. Jochim, Realization of a Laughlin state of two rapidly rotating fermions, Phys. Rev. Lett. **133**, 253401.
[10] A. S. Sørensen, E. Demler, and M. D. Lukin, Fractional quantum Hall states of atoms in optical lattices, Phys. Rev. Lett. **94**, 086803 (2005).
[11] F. A. Palm, M. Buser, J. Léonard, M. Aidelsburger, U. Schollwöck, and F. Grusdt, Bosonic Pfaffian state in the Hofstadter-Bose-Hubbard model, Phys. Rev. B **103**, L161101 (2021).
[12] G. Möller and N. R. Cooper, Composite fermion theory for bosonic quantum Hall states on lattices, Phys. Rev. Lett. **103**, 105303 (2009).
[13] J. Léonard, S. Kim, J. Kwan, P. Segura, F. Grusdt, C. Repellin, N. Goldman, and M. Greiner, Realization of a fractional quantum Hall state with ultracold atoms, Nature **619**, 495 (2023).
[14] N. R. Cooper, Optical flux lattices for ultracold atomic gases, Phys. Rev. Lett. **106**, 175301 (2011).
[15] N. R. Cooper and R. Moessner, Designing topological bands in reciprocal space, Phys. Rev. Lett. **109**, 215302 (2012).
[16] N. R. Cooper and J. Dalibard, Reaching fractional quantum Hall states with optical flux lattices, Phys. Rev. Lett. **110**, 185301 (2013).
[17] P. Lauria, W.-T. Kuo, N. R. Cooper, and J. T. Barreiro, Experimental realization of a fermionic spin-momentum lattice, Phys. Rev. Lett. **128**, 245301 (2022).
[18] J. Wang, J. Cano, A. J. Millis, Z. Liu, and B. Yang, Exact Landau level description of geometry and interaction in a flatband, Phys. Rev. Lett. **127**, 246403 (2021).
[19] P. J. Ledwith, A. Vishwanath, and D. E. Parker, Vortexability: A unifying criterion for ideal fractional Chern insulators, Phys. Rev. B **108**, 205144 (2023).
[20] B. Estienne, N. Regnault, and V. Crépel, Ideal Chern bands as Landau levels in curved space, Physical Review Research **5**, L032048 (2023).
[21] G. Tarnopolsky, A. J. Kruchkov, and A. Vishwanath, Origin of magic angles in twisted bilayer graphene, Phys. Rev. Lett. **122**, 106405 (2019).
[22] Z. Liu, B. Mera, M. Fujimoto, T. Ozawa, and J. Wang, Theory of generalized Landau levels and its implications for non-Abelian states, Physical Review X **15**, 031019 (2025).
[23] M. Fujimoto, D. E. Parker, J. Dong, E. Khalaf, A. Vishwanath, and P. Ledwith, Higher Vortexability: Zero-Field Realization of Higher Landau Levels, Phys. Rev. Lett. **134**, 106502 (2025).
[24] P. J. Ledwith, G. Tarnopolsky, E. Khalaf, and A. Vishwanath, Fractional Chern insulator states in twisted bilayer graphene: An analytical approach, Phys. Rev. Res. **2**, 023237 (2020).
[25] C. Wang, X.-W. Zhang, X. Liu, Y. He, X. Xu, Y. Ran, T. Cao, and D. Xiao, Fractional Chern insulator in twisted bilayer $MoTe_2$, Phys. Rev. Lett. **132**, 036501 (2024).
[26] J. Dong, J. Wang, P. J. Ledwith, A. Vishwanath, and D. E. Parker, Composite Fermi Liquid at Zero Magnetic Field in Twisted $MoTe_2$, Phys. Rev. Lett. **131**, 136502 (2023).
[27] A. P. Reddy, F. Alsallom, Y. Zhang, T. Devakul, and L. Fu, Fractional quantum anomalous Hall states in twisted bilayer $MoTe_2$ and WSe_2, Phys. Rev. B **108**, 085117 (2023).
[28] T. S. Jackson, G. Möller, and R. Roy, Geometric stability of topological lattice phases, Nature Communications **6**, 10.1038/ncomms9629 (2015).
[29] M. Claassen, C. H. Lee, R. Thomale, X.-L. Qi, and T. P. Devereaux, Position-Momentum Duality and Fractional Quantum Hall Effect in Chern Insulators, Phys. Rev. Lett. **114**, 236802 (2015).
[30] B. Mera and T. Ozawa, Engineering geometrically flat Chern bands with Fubini-Study Kähler structure, Phys.

Rev. B **104**, 115160 (2021).
[31] T. Ozawa and B. Mera, Kähler geometry and Chern insulators: Relations between topology and the quantum metric, Phys. Rev. B **104**, 045103 (2021).
[32] N. Morales-Durán, N. Wei, J. Shi, and A. H. MacDonald, Magic angles and fractional chern insulators in twisted homobilayer transition metal dichalcogenides, Phys. Rev. Lett. **132**, 096602 (2024).
[33] Y. Aharonov and A. Casher, Ground state of a spin-1/2 charged particle in a two-dimensional magnetic field, Phys. Rev. A **19**, 2461 (1979).
[34] J. Shi, N. Morales-Durán, E. Khalaf, and A. H. MacDonald, Adiabatic approximation and Aharonov-Casher bands in twisted homobilayer transition metal dichalcogenides, Phys. Rev. B **110**, 035130 (2024).
[35] J. Dalibard, F. Gerbier, G. Juzeliūnas, and P. Öhberg, Colloquium: Artificial gauge potentials for neutral atoms, Rev. Mod. Phys. **83**, 1523 (2011).
[36] N. Goldman, G. Juzeliūnas, P. Öhberg, and I. B. Spielman, Light-induced gauge fields for ultracold atoms, Reports on Progress in Physics **77**, 126401 (2014).
[37] N. R. Cooper, J. Dalibard, and I. B. Spielman, Topological bands for ultracold atoms, Rev. Mod. Phys. **91**, 015005 (2019).
[38] M. V. Berry, Quantal phase factors accompanying adiabatic changes, Proceedings of the Royal Society of London. A. Mathematical and Physical Sciences **392**, 45–57 (1984).
[39] Y. Aharonov and D. Bohm, Significance of electromagnetic potentials in the quantum theory, Phys. Rev. **115**, 485 (1959).
[40] J. Ye, Y. B. Kim, A. J. Millis, B. I. Shraiman, P. Majumdar, and Z. Tešanović, Berry phase theory of the anomalous hall effect: Application to colossal magnetoresistance manganites, Phys. Rev. Lett. **83**, 3737 (1999).
[41] N. R. Cooper and J. Dalibard, Optical flux lattices for two-photon dressed states, Europhysics Letters **95**, 66004 (2011).
[42] F. Wu, T. Lovorn, E. Tutuc, I. Martin, and A. H. MacDonald, Topological insulators in twisted transition metal dichalcogenide homobilayers, Phys. Rev. Lett. **122**, 086402 (2019).
[43] G. Juzeliūnas and I. B. Spielman, Flux lattices reformulated, New Journal of Physics **14**, 123022 (2012).
[44] F. D. M. Haldane, A modular-invariant modified Weierstrass sigma-function as a building block for lowest-Landau-level wavefunctions on the torus, Journal of Mathematical Physics **59** (2018).
[45] S. Nascimbene and J. Dalibard, Emergence of a Landau level structure in dark optical lattices, arXiv:2412.15038 (2024).
[46] B. Li and F. Wu, Variational mapping of Chern bands to Landau levels: Application to fractional Chern insulators in twisted $MoTe_2$, Phys. Rev. B **111**, 125122 (2025).
[47] D. Burba and G. Juzeliūnas, Two dimensional subwavelength topological dark state lattices (2025), arXiv:2506.17096.
[48] L. Chen, T. Mazaheri, A. Seidel, and X. Tang, The impossibility of exactly flat non-trivial Chern bands in strictly local periodic tight binding models, Journal of Physics A: Mathematical and Theoretical **47**, 152001 (2014).
[49] W. Yang, D. Zhai, T. Tan, F.-R. Fan, Z. Lin, and W. Yao, Fractional quantum anomalous Hall effect in a singular flat band, Phys. Rev. Lett. **134**, 196501 (2025).
[50] J. D. Choi, N. Morales-Durán, Y. H. Kwan, A. J. Millis, N. Regnault, and D. Guerci, Higher Chern bands in helical homotrilayer transition metal dichalcogenides, 2507.17819.
[51] N. R. Cooper, Fractional Quantum Hall States of Bosons: Properties and Prospects for Experimental Realization, in *Fractional Quantum Hall Effects* (2020) Chap. Chapter 10, pp. 487–521.
[52] P. Christodoulou, M. Gałka, N. Dogra, R. Lopes, J. Schmitt, and Z. Hadzibabic, Observation of first and second sound in a BKT superfluid, Nature **594**, 191 (2021).
[53] J. L. Ville, T. Bienaimé, R. Saint-Jalm, L. Corman, M. Aidelsburger, L. Chomaz, K. Kleinlein, D. Perconte, S. Nascimbène, J. Dalibard, and J. Beugnon, Loading and compression of a single two-dimensional Bose gas in an optical accordion, Phys. Rev. A **95**, 013632 (2017).
[54] T. H. Hansson, M. Hermanns, S. H. Simon, and S. F. Viefers, Quantum Hall physics: Hierarchies and conformal field theory techniques, Rev. Mod. Phys. **89**, 025005 (2017).
[55] R. B. Laughlin, Anomalous Quantum Hall Effect: An Incompressible Quantum Fluid with Fractionally Charged Excitations, Phys. Rev. Lett. **50**, 1395 (1983).
[56] This has a natural extension to the case of observables which are not diagonal in position basis.
[57] In particular, introduce $\phi \to \lambda\phi$. Then $\partial_\lambda \log[\langle \delta(\mathbf{r}-\mathbf{r}_1)\delta(\mathbf{r}-\mathbf{r}_2)\mathrm{e}^{2\lambda\sum_i \phi}\rangle / \langle \mathrm{e}^{2\lambda\sum_i \phi}\rangle] \simeq 2[2\phi(\mathbf{r}) - \partial_\lambda \log\langle \mathrm{e}^{2\lambda\phi}\rangle]$. The right hand side is a 'mean field' approximation to the true change, as it ignores additional correlation induced by the density modulation.
[58] S. M. Girvin, A. H. MacDonald, and P. M. Platzman, Magneto-roton theory of collective excitations in the fractional quantum Hall effect, Phys. Rev. B **33**, 2481 (1986).
[59] Y. Wang, S. Subhankar, P. Bienias, M. Łą cki, T.-C. Tsui, M. A. Baranov, A. V. Gorshkov, P. Zoller, J. V. Porto, and S. L. Rolston, Dark state optical lattice with a subwavelength spatial structure, Phys. Rev. Lett. **120**, 083601 (2018).
[60] P. Zupancic, P. M. Preiss, R. Ma, A. Lukin, M. E. Tai, M. Rispoli, R. Islam, and M. Greiner, Ultra-precise holographic beam shaping for microscopic quantum control, Opt. Express **24**, 13881 (2016).
[61] N. Read and N. R. Cooper, Free expansion of lowest Landau level states of trapped atoms: A wavefunction microscope, Phys. Rev. A **68**, 035601 (2003).
[62] J. Kwan, P. Segura, Y. Li, T. Blatz, A. Zhi, B. Bakkali-Hassani, A. Bohrdt, M. Greiter, F. Grusdt, and M. Greiner, A Pfaffian quantum Hall state of ultracold bosons, 2606.12409.
[63] M. N. Kosch, L. Asteria, H. P. Zahn, K. Sengstock, and C. Weitenberg, Multifrequency optical lattice for dynamic lattice-geometry control, Physical Review Research **4**, 043083 (2022).
[64] F. D. M. Haldane and E. H. Rezayi, Periodic laughlin-jastrow wave functions for the fractional quantized hall effect, Phys. Rev. B **31**, 2529–2531 (1985).
[65] C. J. Sansonetti, C. E. Simien, J. D. Gillaspy, J. N. Tan, S. M. Brewer, R. C. Brown, S. Wu, and J. V. Porto, Absolute transition frequencies and quantum interference in a frequency comb based measurement of the ^{6,7}Li D lines, Phys. Rev. Lett. **107**, 023001 (2011).

[66] P. Juncar, J. Pinard, J. Hamon, and A. Chartier, Absolute determination of the wavelengths of the sodium D1 and D2 lines by using a CW tunable dye laser stabilized on iodine, Metrologia **17**, 77–79 (1981).
[67] S. Falke, E. Tiemann, C. Lisdat, H. Schnatz, and G. Grosche, Transition frequencies of the d lines of ^{39}K, ^{40}K, and ^{41}K measured with a femtosecond laser frequency comb, Phys. Rev. A **74**, 032503 (2006).
[68] G. P. Barwood, P. Gill, and W. R. C. Rowley, Frequency measurements on optically narrowed Rb-stabilised laser diodes at 780 nm and 795 nm, Applied Physics B Photophysics and Laser Chemistry **53**, 142–147 (1991).
[69] T. Udem, J. Reichert, R. Holzwarth, and T. W. Hänsch, Absolute optical frequency measurement of the cesium d_1 line with a mode-locked laser, Phys. Rev. Lett. **82**, 3568 (1999).
[70] T. Udem, J. Reichert, T. W. Hänsch, and M. Kourogi, Absolute optical frequency measurement of the cesium D_2 line, Phys. Rev. A **62**, 031801 (2000).
[71] U. Volz and H. Schmoranzer, Precision lifetime measurements on alkali atoms and on helium by beam–gas–laser spectroscopy, Physica Scripta **1996**, 48 (1996).
[72] J. M. Amini and H. Gould, High precision measurement of the static dipole polarizability of cesium, Phys. Rev. Lett. **91**, 153001 (2003).

Appendix A: Further Exact Diagonalization Results

Beyond what is shown in the main text, we emphasize that the existence of FQH states is generic to our models, and their spectra closely resemble those of the LLL. Consider Figure 9, where dispersionless exact diagonalization results for $N_\phi = 12$ and $N_B = 6, 8, 9, 12$ are shown, in the first 3 cases for each of the 1-flat dual Haldane, triangular and square models, and in the last case only for the dual Haldane and triangular models. Alongside these we show the LLL spectrum in the same super-cell geometries, and as can be clearly observed, the agreement is remarkable. This is especially so in the case of the dual square and triangular models, while there are visible splittings in the case of the dual Haldane model. The calculations are carried out for $V^{\triangle}$ at parameters $(V_0, V_1) = (1.39, 10.55)\omega_c$, and for $V^{\square}$ at $(V_+, V_z, V_0) = (4.88, 4.04, 0)\omega_c$, while $V^{\hexagon}$ is at the aforementioned parameter point with a C_6 symmetry super-cell. In all models we see clear many-body gaps for $\nu = 1/2, 2/3, 3/4$ with ground state degeneracy $2, 3, 4$ consistent with the bosonic Jain sequence at filling $\nu = p/(p+1)$ for $p = 1, 2, 3$, which is further supported by the near-exact match between the model and LLL spectra. At filling $\nu = 1$ the emergent composite fermions feel no average effective magnetic field. There is a competition between charge ordering into stripes, and pairing, the latter of which results in the Moore-Read state. This competition and the large correlation length are evident from how sensitive the spectra are to the super-cell geometry. For the dual Haldane model, in a C_6 symmetric super-cell, a clear 3-fold degenerate ground state occurs at the Brillouin zone origin. By contrast, the triangular model does display 3 low-lying states, but they are far from degenerate. In the square case no ground state manifold is apparent in any super-cell geometry we have tried, so we do not display the spectra. Still, in all cases, especially the square and triangular models, the spectra are a near-exact match for those of the LLL, for which it is known that the ground state is the Moore-Read state. Thus we have confidence that the split degeneracy is a finite size effect, and that the physics of the LLL survives essentially unmodified in these ideal bands.

The phase transitions between the superfluid and FQH states are governed by the competition between the single particle and interaction energies. We study 4×4 supercells with $N_B = 8$ bosons in the lowest band in the aforementioned 1-flat models, along with the 2-flat dual square model at parameters $(V_+, V_z, V_0) = (4.19, 3.77, 0.87)\omega_c$. As can be seen in Fig. 10, the phase transition to the Laughlin state occurs in the 1-flat dual Haldane and square models around $\tilde{g} \simeq 0.15 - 0.2$ while it occurs in the 2-flat dual square and the 1-flat dual triangular model at the much smaller $\tilde{g} \simeq (3 - 5) \times 10^{-4}$. While this is interesting from the point of view of reaching strong correlations, it is likely that effects beyond the bandwidth would limit the observation of the Laughlin state for too small many body gaps, which puts an effective lower limit

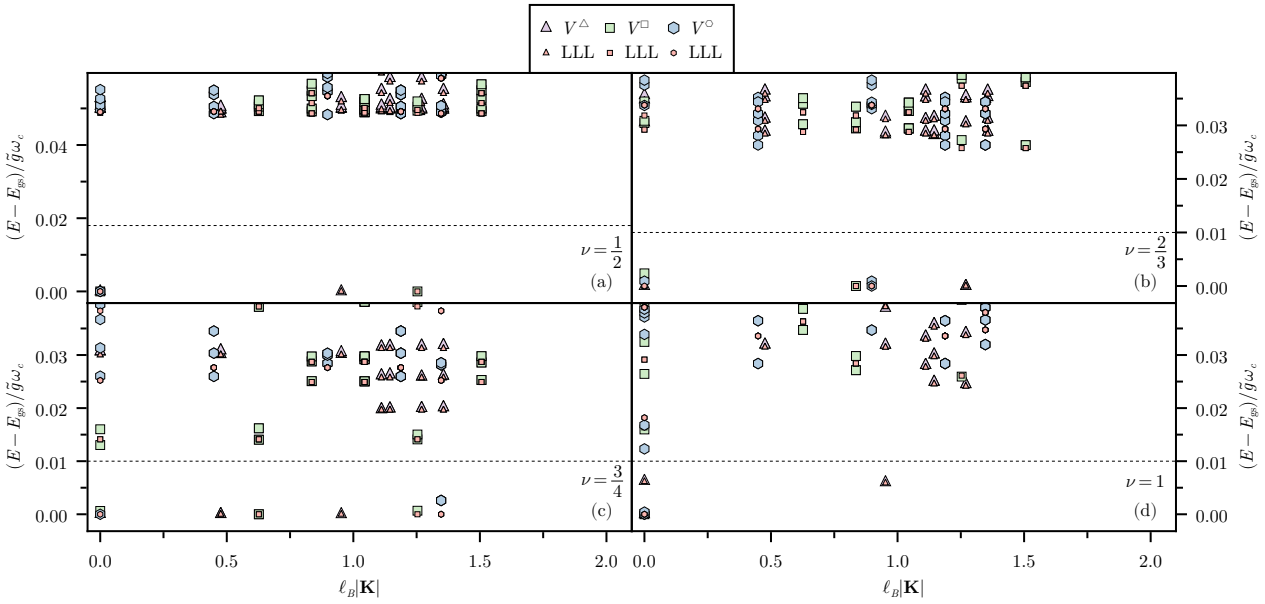


FIG. 9. Many body ED spectra of dual Haldane, square and triangular models in the dispersionless limit, along with that for the LLL in the same lattice geometries. The dashed lines separate ground states from excited states, and we note that we have subtracted the ground state energy in all cases. The panels correspond to (a) $\nu = 1/2, N_B = 6$, showing 2-fold ground state degeneracy (b) $\nu = 2/3, N_B = 8$ showing 3-fold ground state degeneracy (c) $\nu = 3/4, N_B = 9$ showing 4-fold ground state degeneracy and (d) $\nu = 1, N_B = 12$ showing 3-fold ground state degeneracy.

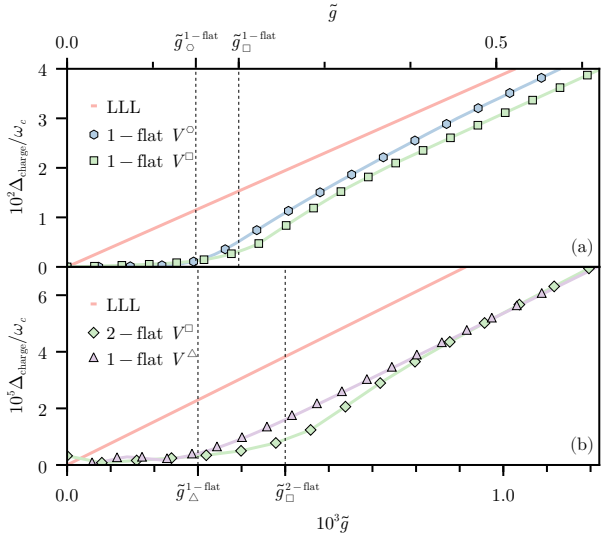


FIG. 10. Charge gap for the superfluid-Laughlin state transition at $\nu = 1/2$ computed for $N_B = 8$ bosons. We also include the genuine LLL charge gap, which is directly proportional to $\tilde{g}$.

on $\tilde{g}$ regardless of the transition point.

Appendix B: Experimental schemes

For state-dependent optical lattices, the choice of two internal states has large experimental implications on the preparation and lifetime of the experiment. In keeping with the nature of the flat bands, our considerations here are general, and should be considered merely an example for a possible experimental procedure. Consider a ground state manifold characterized by definite combined orbital and spin angular momentum J and nuclear spin I, so that in the absence of magnetic field the manifold splits further into levels of definite total angular momentum $F = |I - J|, \ldots, I + J$. In the case of alkali-metal atoms, the ground state has $J = 1/2$. For fermionic isotopes F is half-integer while for bosonic isotopes it is integer. Furthermore, applying a small quantizing magnetic field, which we take to be in the vertical z direction, the energy levels may be labeled $|F, m_F\rangle$.

Increasing the magnetic field until the quadratic Zeeman effect detunes the atomic transitions by energies in large excess of ω_c, a two-level system can be furnished from a pair $|\pm\rangle = |F_{\pm}, m_{\pm}\rangle$. Let us focus on the case of off-resonant lasers, so that the optical lattice potential arises from the second order light shift. This is controlled by the dynamic polarizability tensor operator α_{ab} of the ground state manifold, that is characterized by a combination of scalar α_S, vector α_V, and tensor α_T components.

For each frequency ω, this decomposition becomes

$$\alpha_{ab}(\omega) = \alpha_S(\omega)\delta_{ab} - \alpha_V(\omega)\frac{\mathrm{i}\epsilon_{abc}\hat{J}_c}{2J} + \alpha_T(\omega)\frac{3[\hat{J}_a\hat{J}_b + \hat{J}_b\hat{J}_a] - 2\delta_{ab}\hat{\mathbf{J}}^2}{2J(2J-1)} \tag{B1}$$

where for notational clarity the $\hat{}$ have been added on angular momentum operators. Generically $\alpha_{ab}(\omega)$ is predominantly real, but has a finite imaginary component. This is the remnant of the finite life time of the excited states which the light field mixes with the ground state.

1. Alkali Metals

Projected to within the $|\pm\rangle$ subspace, the polarizability need not take a form as elegant as (B1). Let us initially focus on the situation where $\alpha_T = 0$, as is appropriate for alkali-metals, notably Rubidium and Cesium. Since the vector polarizability allow for off-diagonal matrix elements differing by at most 1 unit of angular momentum, the states $|\pm\rangle$ must be chosen such that $|m_+ - m_-| \leq 1$ to have any hope for creating an OFL. Naturally this leads to two qualitatively different kinds of OFL designs coherent with the choice of schemes

V1 $m_+ = m_- + 1$, while $F_\pm = F$ ($F_+ \neq F_-$ is perfectly possible but we don't consider it).

V2 $m_+ = m_- = m$ while $F_\pm = I \pm 1/2$

Scheme V1 has the advantage of not suffering two-body hyperfine relaxation in collisions, but we often find simpler setups using scheme V2, and in the Laughlin state, collisions are strongly suppressed, likely making hyperfine relaxation an unimportant source of atomic loss. In the first scheme V1, all three angular momentum operators have non-trivial projector onto the two-level system

$$\hat{J}_3 \overset{\text{V1}}{\mapsto} 2J(A + B\hat{\sigma}_3) \tag{B2}$$

$$\hat{J}_{1,2} \overset{\text{V1}}{\mapsto} 2JC\hat{\sigma}_{1,2} \tag{B3}$$

for three constants A, B, C. Ignoring the mixing caused by finite magnetic field, these coefficients can be easily worked out

$$B = \frac{F(F+1) + J(J+1) - I(I+1)}{8JF(F+1)} \tag{B4}$$

$$A = (2m_- + 1)B \tag{B5}$$

$$C = B\sqrt{F(F+1) - m_-m_+} \tag{B6}$$

Importantly for bosonic isotopes, there is no possible choice of levels within scheme V1, such that $A = 0$ for small magnetic fields. This conclusion is not altered by considering states from different $F_+ \neq F_-$. For fermionic isotopes such a pair of states could be $m_F = \pm 1/2$. This form leads to the projected polarizability

$$\alpha_{ab} \overset{\text{V1}}{\mapsto} \alpha_S\delta_{ab} - \mathrm{i}A\alpha_V\epsilon_{ab} - \mathrm{i}B\alpha_V\hat{\sigma}_3\epsilon_{ab} - \mathrm{i}C\alpha_V\epsilon_{abc}\hat{\sigma}_{c\perp} \tag{B7}$$

which shows the unfortunate reality that the vector shift $\hat{\sigma}_3$ will be accompanied by a scalar component. This scalar component is furthermore phase-shifted relative to the usual scalar component, which often leads to undesirable effects, and can make it hard to cancel. Consider for example the laser setup of Ref. [41] realizing the dual Haldane model when $A = 0$. The two levels are split in energy by δ, and the setup consists of three planar lasers with frequency ω, amplitude $\mathcal{E}$ and polarization angle θ to the vertical, as well as a vertical circularly polarized laser of frequency $\omega + \delta$ and amplitude $r\mathcal{E}$

$$\mathbf{E}_\omega = \mathcal{E}\sum_a (\cos\theta\mathbf{e}_z + \sin\theta\hat{\mathbf{q}}_a \wedge \mathbf{e}_z)\mathrm{e}^{\mathrm{i}\mathbf{q}_a\cdot\mathbf{r}} \tag{B8}$$

$$\mathbf{E}_{\omega+\delta} = r\mathcal{E}\mathrm{e}^{\mathrm{i}|\mathbf{q}|\mathbf{e}_z\cdot\mathbf{r}}\frac{\mathbf{e}_x + \mathrm{i}\mathbf{e}_y}{\sqrt{2}} \tag{B9}$$

In the rotating frame, the total potential takes a form $V^{\hexagon} + V^{\text{const.}}$ with parameters:

$$V_0 = -\frac{\alpha_S(3\cos^2\theta - 1) - \alpha_V\mathrm{i}\sqrt{3}A\sin^2\theta}{2}\mathcal{E}^2 \tag{B10}$$

$$V_+ = -\alpha_V Cr\sqrt{2}\cos\theta\mathcal{E}^2 \tag{B11}$$

$$V_z = \frac{\alpha_V B\sqrt{3}\sin^2\theta}{2}\mathcal{E}^2 \tag{B12}$$

$$V^{\text{const.}} = -(3 + r^2)\alpha_S\mathcal{E}^2 \tag{B13}$$

Recall the illustration of the dual Haldane model in Fig. 2. When V_0 is not purely real, the two sublattices in the dual Haldane model experience unequal reciprocal space flux. This breaks the C_6 symmetry, making it impossible to reach the 1-flat manifold by tuning a single parameter. When $A \neq 0$ there is no way to avoid this with this particular setup. Under scheme V2, we find that

$$J_3 \overset{\text{V2}}{\mapsto} \tilde{C}\hat{\sigma}_1 + \tilde{B}\hat{\sigma}_3 \qquad J_{1,2} \overset{\text{V2}}{\mapsto} 0 \tag{B14}$$

where

$$|\tilde{C}| = \frac{\sqrt{(I+1/2)^2 - m^2}}{2I+1} \tag{B15}$$

$$\tilde{B} = \frac{m}{2I+1} \tag{B16}$$

While $J_{1,2} \mapsto 0$ does impose some design limitations, they are not so severe as to prevent the creation of OFL. Under V2 the polarizability takes the form

$$\alpha_{ab} \overset{\text{V2}}{\mapsto} \alpha_S\delta_{ab} - \mathrm{i}\tilde{B}\hat{\sigma}_3\alpha_V\epsilon_{ab} - \mathrm{i}\tilde{C}\alpha_V\hat{\sigma}_1\epsilon_{ab} \tag{B17}$$

Independent control of the different vector components of the potential are possible since only resonant beams contribute to the optical potential, but more complicated optical setups than previously considered are often still necessary.

2. Dual Haldane Model for bosons in scheme V1

One possibility to realize the dual Haldane model is by using multiple frequencies for the planar lasers. Such

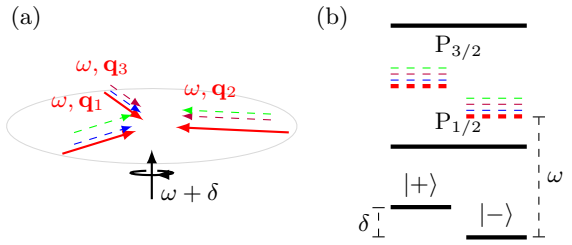


FIG. 11. (a) The imagined optical setup for the dual Haldane model in bosonic atoms under scheme V1. There is one circularly polarized out-of-plane laser, and three main in-plane lasers. Each main laser has two different side bands as indicated by the color, which are detuned by an electro-optical modulator as in [63]. See equation (B20) (b) Level diagram showing the two internal states, the virtual levels dressed by the laser frequencies, as well as the excited P levels from which the polarizability derives.

a multi frequency scheme was practically realized using electro-optical modulators in [63]. In particular, consider a scheme involving a main frequency ω, along with sidebands $\omega_{1,2,3}$ and an out-of-plane laser with frequency $\omega+\delta$, as illustrated in Fig. 11

$$\mathbf{E}_{\omega} = \mathcal{E}\sum_a (\cos\theta \mathbf{e}_z + \sin\theta \hat{\mathbf{q}}_a \wedge \mathbf{e}_z) e^{i\mathbf{q}_a\cdot\mathbf{r}} \tag{B18}$$

$$\mathbf{E}_{\omega_a} = r_{\parallel}\mathcal{E}\mathbf{e}_z[e^{i\mathbf{q}_{a+1}\cdot\mathbf{r}+i\phi} + e^{i\mathbf{q}_a\cdot\mathbf{r}}] \tag{B19}$$

$$\mathbf{E}_{\omega+\delta} = r\mathcal{E}e^{i|\mathbf{q}|\mathbf{e}_z\cdot\mathbf{r}}\frac{\mathbf{e}_x + i\mathbf{e}_y}{\sqrt{2}}. \tag{B20}$$

There is great flexibility in how to distribute the scalar potential between the side and main frequency, with simplest being that $\phi = \pi/2$ (or $-\pi/2$ corresponding to the sign of $\alpha_V A/\alpha_S$), and that

$$\alpha_S r_{\parallel}^2 = \frac{\sqrt{3}\sin^2\theta A\alpha_V}{2} \tag{B21}$$

Then the parameters V_0, V_+, V_z of the dual Haldane model become

$$V_0 = -\frac{3\cos^2\theta - 1}{2}\alpha_S\mathcal{E}^2 \tag{B22}$$

$$V_+ = r\sqrt{2}\cos\theta C\alpha_V\mathcal{E}^2 \tag{B23}$$

$$V_z = \frac{\sqrt{3}\sin^2\theta}{2}B\alpha_V\mathcal{E}^2 \tag{B24}$$

The overall constant of the potential has an imaginary part given by

$$\mathrm{Im}V^{\mathrm{const.}} = \left[-(3+r^2) - 3^{3/3}\sin^2\theta A\frac{\alpha_V}{|\alpha_S|}\right]\mathrm{Im}\alpha_S\mathcal{E}^2 \tag{B25}$$

This term is the dominant source of heating in the lattice when $\alpha_S \gg \alpha_V$. In this regime, the scalar lattice strength is largely irrelevant for the heating calculation, and the beams must be close to orthogonal so that $\cos\theta \sim 1/3$.

The overall heating is dominated by the uniform background potential

$$\mathrm{Im}V^{\mathrm{const.}} \approx -\left(3\sqrt{3} + \frac{B^2V_+^2}{C^2V_z^2}\right)\frac{V_z}{|B|}\frac{\mathrm{Im}\alpha_S}{\alpha_V} \tag{B26}$$

For any particular parameter point of the dual Haldane model, the far detuned heating is limited by the ratio $\mathrm{Im}\,\alpha_S/\alpha_V$ which tends to $3\Gamma/4(\omega_{3/2}-\omega_{1/2})$, see Appendix E for details. Consider the 1-flat parameter point from IV, where $(V_z, V_+, V_0) = (3.06, 7.06, 2.09)\omega_c$. The heating is similar for any choice of $m_\pm$, so for simplicity let $m_- = -F$. Then the inverse lifetime for

$$\Gamma^{\gamma} \simeq \left(3\sqrt{3} + \frac{5.3}{2I-1}\right)\frac{9.2\omega_c\Gamma(2I+1)}{\omega_{3/2}-\omega_{1/2}} \tag{B27}$$

$$= \frac{\Gamma\omega_c}{\omega_{3/2}-\omega_{1/2}} \times \begin{cases} 144 & I = 3/2 \\ 180 & I = 5/2 \\ 223 & I = 7/2 \end{cases} \tag{B28}$$

For ^{87}Rb with $I = 3/2$ and using the values from II, we find $\Gamma^{\mathrm{asymp}} = 5.6\times10^{-4}\omega_c$. At the red-detuned wavelength $\lambda = 810\,\mathrm{nm}$ we have $\omega_c = 2\pi\times 2.9\,\mathrm{kHz}$, so $\Gamma^{\mathrm{asymp}} \simeq 1.6\,\mathrm{s}^{-1}$, while for ^{133}Cs where $I = 7/2$ a red detuned laser of wavelength $\lambda = 950\,\mathrm{nm}$ we have $\omega_c = 2\pi\times 1.3\,\mathrm{kHz}$, while $\Gamma^{\mathrm{asymp}} = 3.1\times10^{-4}\omega_c$, and hence $\Gamma^{\mathrm{asymp}} \simeq 0.4\,\mathrm{s}^{-1}$. We note that while the heating rate for Rubidium is significantly larger, which is primarily due to the increased recoil energy. As such, for a fixed $\tilde{g}$ the ratio between the many body gaps and the decay rate, which is what ultimately determines the stability of the state, differs much less in the two cases.

3. Dual Haldane Model in scheme V2

Alternatively, we can pick a manifold of constant m_F but containing two different $F_\pm = I \pm 1/2$, so that $J_3 \mapsto \tilde{C}\hat{\sigma}_1 + \tilde{B}\hat{\sigma}_3, J_{1,2} \mapsto 0$. In this case, consider a laser setup with two main frequencies $\omega, \tilde{\omega}$ for in-plane lasers, and a single out-of-plane laser at frequency $\omega+\delta$:

$$\mathbf{E}_{\omega} = \mathcal{E}\sum_a e^{\frac{2\pi i a}{3}}(\cos\theta\mathbf{e}_z + \sin\theta\hat{\mathbf{q}}_a\wedge\mathbf{e}_z)e^{i\mathbf{q}_a\cdot\mathbf{r}} \tag{B29}$$

$$\mathbf{E}_{\tilde{\omega}} = \mathcal{E}\sum_a e^{-\frac{2\pi i a}{3}}(\cos\theta\mathbf{e}_z + \sin\theta\hat{\mathbf{q}}_a\wedge\mathbf{e}_z)e^{i\mathbf{q}_a\cdot\mathbf{r}} \tag{B30}$$

$$\mathbf{E}_{\omega+\delta} = r\mathcal{E}e^{i|\mathbf{q}|\mathbf{e}_z\cdot\mathbf{r}}\frac{\mathbf{e}_x + i\mathbf{e}_y}{\sqrt{2}}. \tag{B31}$$

This results in the lattice potential of a dual Haldane model with

$$V^{\mathrm{const}} = -(6+r^2)\alpha_S\mathcal{E}^2 \tag{B32}$$

$$V_0 = -(3\cos^2\theta - 1)\alpha_S\mathcal{E}^2 \tag{B33}$$

$$V_+ = -r\sqrt{2}\cos\theta\tilde{C}\alpha_V\mathcal{E}^2 \tag{B34}$$

$$V_z = \frac{\sqrt{3}\sin^2\theta\tilde{B}\alpha_V}{2}\mathcal{E}^2 \tag{B35}$$

Again, it is the constant piece of the potential that is the biggest source of heating when $\alpha_S \gg \alpha_V$,

$$\operatorname{Im} V^{\text{const.}} = -\left(6 + \frac{V_+^2 \tilde{B}^2}{2V_z^2 \tilde{C}^2}\right) \frac{V_z \sqrt{3} \operatorname{Im} \alpha_S}{\tilde{B} \alpha_V} \tag{B36}$$

For $m_- = -F$ we find for the same parameters as before in ^{87}Rb a heating rate $\Gamma^{\text{asymp}} = 2\,\text{s}^{-1}$, while for ^{133}Cs we find $\Gamma^{\text{asymp}} = 0.2\,\text{s}^{-1}$.

4. Dual Square model under scheme V2

Consider the optical lattice generated by a light field with frequencies $\omega, \omega + \delta$ where δ is the splitting between $|\pm\rangle$. We consider a quartet of wavevectors $\mathbf{q}_a = q\mathbf{e}_x \cos\frac{\pi a}{2} + q\mathbf{e}_y \sin\frac{\pi a}{2}$ where the a index is an integer mod 4. The electric field components take the form

$$\mathbf{E}_\omega = \frac{\mathcal{E}}{\sqrt{2}} \sum_a \mathrm{e}^{\frac{\mathrm{i}\pi a}{2}} (\mathrm{e}^{\mathrm{i}\phi} \mathbf{e}_z + \hat{\mathbf{q}}_{a+1}) \mathrm{e}^{\mathrm{i}\mathbf{q}_a \cdot \mathbf{r}} \tag{B37}$$

$$\mathbf{E}_{\omega+\delta} = \frac{r\mathcal{E}}{\sqrt{2}} \mathrm{e}^{\mathrm{i}|\mathbf{q}|\mathbf{e}_z \cdot \mathbf{r}} (\mathbf{e}_x + \mathbf{e}_y) \tag{B38}$$

where ϕ is a free parameter that does not impact the resulting potential, but may make experimental design more straightforward. The resulting scalar potential is a constant

$$V^{\text{const.}} = (4 + |r|^2) \mathcal{E}^2 \alpha_S \tag{B39}$$

while the spatially dependent potential takes the form of the π-square model (12) with

$$V_z = \mathcal{E}^2 \alpha_V \tilde{B} \tag{B40}$$

$$V_+ = \frac{r\mathcal{E}^2 \alpha_V \tilde{C}}{2} \tag{B41}$$

$$V_0 = 0 \tag{B42}$$

Even without utilizing the additional scalar parameter we can reach the 1-flat condition. An additional scalar potential as prescribed by the model can be included using beams of wavevector $2\mathbf{q}_a$ at frequency 2ω. When the electric field has the form

$$\mathbf{E}_{2\omega} = \frac{\tilde{r}\mathcal{E}}{\sqrt{2}} \sum_a (\mathrm{e}^{\mathrm{i}\tilde{\phi}} \mathbf{e}_z + \hat{\mathbf{q}}_{a+1}) \mathrm{e}^{2\mathrm{i}\mathbf{q}_a \cdot \mathbf{r}} \tag{B43}$$

for some common phase $\mathrm{e}^{\mathrm{i}\tilde{\phi}}$. This additional light field creates a scalar potential of the form

$$\alpha_S(2\omega) \tilde{r}^2 \mathcal{E}^2 \left(4 + \sum_a \mathrm{e}^{2\mathrm{i}(\mathbf{q}_{a+1} - \mathbf{q}_a)}\right) \tag{B44}$$

while the interference cancels any vector shift. The resulting model is then the π-square model with

$$V^{\text{const.}} = \mathcal{E}^2([4 + r^2]\alpha_S(\omega) + 4\tilde{r}^2 \alpha_S(2\omega)) \tag{B45}$$

$$V_z = \mathcal{E}^2 \tilde{B} \alpha_V(\omega) \tag{B46}$$

$$V_+ = \frac{r\mathcal{E}^2 \tilde{C} \alpha_V(\omega)}{2} \tag{B47}$$

$$V_0 = \mathcal{E}^2 \tilde{r}^2 \alpha_S(2\omega) \tag{B48}$$

In the regime of interest $\alpha_S \gg \alpha_V$, while $V_0 \sim V_+$, so $\tilde{r} \ll 1$, and the additional heating from the scalar lattice is completely negligible. The heating rate takes the form

$$\Gamma^\gamma \simeq -\frac{8 V_z \operatorname{Im} \alpha_S}{\tilde{B} \alpha_V} \left[1 + \frac{V_+^2 \tilde{B}^2}{V_z^2 \tilde{C}^2}\right] \tag{B49}$$

At the 2-flat parameter point $(V_+, V_z, V_0) = (4.19, 3.77, 0.87)\omega_c$, we find an asymptotic heating rate of $\Gamma^{\text{asymp}} \simeq 0.8\,\text{s}^{-1}$ at $\lambda = 810\,\text{nm}$ in ^{87}Rb, while at $\lambda = 950\,\text{nm}$ in ^{133}Cs it becomes $\Gamma^{\text{asymp}} \simeq 0.1\,\text{s}^{-1}$.

Appendix C: Landau level review

For convenience we give a short review of Landau levels on a plane in the periodic basis[64]. Consider the usual affine plane $\mathbb{R}^2$ with coordinates x^1, x^2 and magnetic field F_{ab}, which is related to the flux density B by the antisymmetric tensor $F_{ab} = \epsilon_{ab} B$. We consider identical charge $+1$ particles moving on the plane. When these are transported around the plane, they acquire an Aharonov-Bohm phase. The generator of this translation is the kinetic momentum $\boldsymbol{\pi}$, which has the form $\pi_a = -\mathrm{i}\nabla_a - A_a$ where A_a is the connection. The operator commutation relations take the form

$$[x^a, x^b] = 0 \qquad [x^a, \pi_b] = \mathrm{i}\delta^a_b \qquad [\pi_a, \pi_b] = \mathrm{i}F_{ab}. \tag{C1}$$

Even without specifying a particular Hamiltonian, it is natural to ponder the existence of operators that commute with both $\pi_{1,2}$. When B is constant (C1) is a central extension of the usual Heisenberg algebra, and we may construct such operators, which are the guiding center momenta $\tilde{\pi}_a = \pi_a - F_{ab} x^b$. Their name is chosen since $R^a = \epsilon^{ab} \tilde{\pi}_b / B$ are the typical guiding center operators. The two kinds of momenta commute

$$[\tilde{\pi}_a, \pi_b] = \mathrm{i}F_{ab} - F_{ac}[x^c, \pi_b] = \mathrm{i}F_{ab} - \mathrm{i}F_{ab} = 0 \tag{C2}$$

while the guiding center momenta have opposite chirality to π_a

$$[\tilde{\pi}_a, \tilde{\pi}_b] = -\mathrm{i}F_{ab} \tag{C3}$$

The guiding center momenta are distinct from the kinetic momenta, and as such there are two natural notions of translation operators. The parallel transport translations $t(\mathbf{d}) = \mathrm{e}^{\mathrm{i}\mathbf{d}\cdot\boldsymbol{\pi}}$ and the guiding center translations

$\hat{t}(\mathbf{d}) = \mathrm{e}^{\mathrm{i}\mathbf{d}\cdot\hat{\boldsymbol{\pi}}}$. Since they have the same commutation relations with the position operator $\mathbf{x}$, if $V(\mathbf{x})$ is an operator $t^\dagger(\mathbf{d})V(\mathbf{x})t(\mathbf{d}) = \hat{t}^\dagger(\mathbf{d})V(\mathbf{x})\hat{t}(\mathbf{d}) = V(\mathbf{x}-\mathbf{d})$. Their translation algebras are inherited from their respective momentum algebras

$$t(\mathbf{d}_1)t(\mathbf{d}_2) = t(\mathbf{d}_1+\mathbf{d}_2)\mathrm{e}^{-\frac{\mathrm{i}}{2}F_{ab}d_1^a d_2^b} \tag{C4}$$

whereas

$$\hat{t}(\mathbf{d}_1)\hat{t}(\mathbf{d}_2) = \hat{t}(\mathbf{d}_1+\mathbf{d}_2)\mathrm{e}^{+\frac{\mathrm{i}}{2}F_{ab}d_1^a d_2^b}. \tag{C5}$$

Let us suppose magnetic field or potential inhomogeneities conspire so that only translations along some lattice $\Lambda = \mathbf{a}_1\mathbb{Z}\oplus\mathbf{a}_2\mathbb{Z}$ are symmetries, with a unit cell that encloses 2π flux $F_{ab}a_1^a a_2^b = 2\pi$. The dual lattice we denote $\Lambda^\star = \mathbf{g}_1\mathbb{Z}\oplus\mathbf{g}_2\mathbb{Z}$, where $\mathbf{g}_a^i = \epsilon^{ij}F_{ab}\mathbf{a}_j^b$. This ensures that the corresponding guiding center translations commute $\hat{t}(\mathbf{a}_1)\hat{t}(\mathbf{a}_2) = \hat{t}(\mathbf{a}_2)\hat{t}(\mathbf{a}_1)$, hence they can be simultaneously diagonalized. This motivates defining their common eigenstates, which are essentially the magnetic Bloch wave-functions, with crystal momenta $\mathbf{k}$ by

$$\hat{t}(\mathbf{a}_i)\left|\mathbf{k}\right\rangle = -\mathrm{e}^{\mathrm{i}\mathbf{a}_i\cdot\mathbf{k}}\left|\mathbf{k}\right\rangle \tag{C6}$$

in analogy with the usual translation symmetry. The choice of overall $-$ sign corresponds to a shift in the origin of the Brillouin zone, which is made since it makes the resulting wave-functions more symmetric between real and momentum space. With this preamble, let us understand the magnetic Bloch wave-functions. To write these down explicitly, we must pick a gauge connection. For example the symmetric gauge wherein $A_a = -\frac{1}{2}F_{ab}x^b$, and hence $\tilde{\pi}_a = -\mathrm{i}\nabla_a - \frac{1}{2}F_{ab}x^b$. Consider first understanding the eigenstates of $\mathbf{a}_1\cdot\hat{\boldsymbol{\pi}}$ with eigenvalue $2\pi\phi_1$. These eigenstates satisfy

$$2\pi\phi_1 f_{\phi_1}(\mathbf{x}) = \left(-\mathrm{i}\mathbf{a}_1\cdot\nabla - \frac{\epsilon_{1j}}{2}\mathbf{g}^j\cdot\mathbf{x}\right)f_{\phi_1}(\mathbf{x}) \tag{C7}$$

which can be directly integrated to yield

$$f_{\phi_1}(\mathbf{x}) = \mathrm{e}^{\mathrm{i}\phi_1\mathbf{x}\cdot\mathbf{g}^1 + \frac{\mathrm{i}\epsilon_{12}}{4\pi}(\mathbf{g}^2\cdot\mathbf{x})(\mathbf{g}^1\cdot\mathbf{x})} \tag{C8}$$

up to a multiplicative function dependent only on $\mathbf{g}^2\cdot\mathbf{x}$. Since the guiding center translations by $\mathbf{a}_{1,2}$ commute, we can form a superposition of f_{ϕ_1+n} for $n\in\mathbb{Z}$ states that are $\hat{t}(\mathbf{a}_2)$ eigenstates. It is straightforward to compute the action of $\hat{t}(\mathbf{a}_2)$ on f_{ϕ_1}

$$\hat{t}(\mathbf{a}_2)f_{\phi_1}(\mathbf{x}) = \mathrm{e}^{\mathrm{i}\mathbf{g}^1\cdot\mathbf{x}}f_{\phi_1}(\mathbf{x}) = f_{\phi_1+1}(\mathbf{x}) \tag{C9}$$

The most general eigenstate of $\hat{t}(\mathbf{a}_{1,2})$ with eigenvalues $\mathrm{e}^{\mathrm{i}2\pi\phi_{1,2}}$ must be a superposition of the form

$$\chi(\mathbf{x}) = \sum_{n\in\mathbb{Z}} f_{\phi_1+n}(\mathbf{x})h_n(\mathbf{g}^2\cdot\mathbf{x}) \tag{C10}$$

where h_n is some set of functions. To find conditions relating h_n we investigate the action of $\hat{t}(\mathbf{a}_2)$. In particular

$$\mathrm{e}^{\mathrm{i}2\pi\phi_2}\chi = \hat{t}(\mathbf{a}_2)\chi_{\phi_1,\phi_2} = \sum_n f_{\phi_1+n+1}(\mathbf{x})h_n(\mathbf{g}^2\cdot\mathbf{x}+2\pi) \tag{C11}$$

From the linear independence of the summand, it is clear $\mathrm{e}^{\mathrm{i}2\pi\phi_2}h_n(\mathbf{g}^2\cdot\mathbf{x}) = h_{n-1}(\mathbf{g}^2\cdot\mathbf{x}+2\pi)$, which immediately implies

$$h_n(\mathbf{g}^2\cdot\mathbf{x}) = \mathrm{e}^{-\mathrm{i}2\pi\phi_2 n}\tilde{h}(\mathbf{g}^2\cdot\mathbf{x}+2\pi n) \tag{C12}$$

for an arbitrary function $\tilde{h}$. In particular let us factor out $\tilde{h} = \mathrm{e}^{\mathrm{i}\phi_2\mathbf{g}^2\cdot\mathbf{x}}h$. In terms of this arbitrary function, the simultaneous eigenfunctions take the form

$$\chi_{\phi_1\phi_2}(\mathbf{x}) = \mathrm{e}^{\mathrm{i}\phi_i\mathbf{g}^i\cdot\mathbf{x}+\frac{\mathrm{i}}{4\pi}(\mathbf{g}^1\cdot\mathbf{x})(\mathbf{g}^2\cdot\mathbf{x})}\sum_{n\in\mathbb{Z}}\mathrm{e}^{\mathrm{i}n\mathbf{g}^1\cdot\mathbf{x}}h(\mathbf{g}^2\cdot\mathbf{x}+2\pi n)$$

This is naively very asymmetric between the two lattice vectors, but they can be related by Poisson resummation, which exchange $\mathbf{g}^{1,2}$ and replaces h with its Fourier transform. In particular the Fourier series of the Dirac comb can be expressed

$$\sum_{n\in\mathbb{Z}}\delta(x-2\pi n) = \frac{1}{2\pi}\sum_{n\in\mathbb{Z}}\mathrm{e}^{\mathrm{i}nx} \tag{C13}$$

$$= \sum_{n\in\mathbb{Z}}\int_{\mathbb{R}}\frac{\mathrm{d}y}{2\pi}\mathrm{e}^{\mathrm{i}xy/2\pi}\delta(y-2\pi n) \tag{C14}$$

Defining $\hat{h}(y) = \int \mathrm{d}x\mathrm{e}^{\mathrm{i}xy/2\pi}h(x)/2\pi$ Poisson resummation relates

$$\sum_{n\in\mathbb{Z}}\mathrm{e}^{\mathrm{i}n\mathbf{g}_1\cdot\mathbf{x}}h(\mathbf{g}^2\cdot\mathbf{x}+2\pi n) \tag{C15}$$

$$= \int\mathrm{d}\theta\sum_{n\in\mathbb{Z}}\mathrm{e}^{\mathrm{i}\theta\mathbf{g}^1\cdot\mathbf{x}/2\pi}h(\theta)\delta(\theta-2\pi n) \tag{C16}$$

$$= \sum_{n\in\mathbb{Z}}\int\frac{\mathrm{d}\theta\mathrm{d}\phi}{2\pi}\mathrm{e}^{\mathrm{i}\theta(\phi+\mathbf{g}^1\cdot\mathbf{x})/2\pi}h(\mathbf{g}^2\cdot\mathbf{x}+\theta)\delta(\phi-2\pi n) \tag{C17}$$

$$= \mathrm{e}^{-\frac{\mathrm{i}}{2\pi}(\mathbf{g}^1\cdot\mathbf{x})(\mathbf{g}^2\cdot\mathbf{x})}\sum_{n\in\mathbb{Z}}\hat{h}(\mathbf{g}^1\cdot\mathbf{x}+2\pi n)\mathrm{e}^{-\mathrm{i}n\mathbf{g}^2\cdot\mathbf{x}} \tag{C18}$$

so we could equally well write

$$\chi_{\phi_1\phi_2} = \mathrm{e}^{\mathrm{i}\phi_i\mathbf{g}^i\cdot\mathbf{x}-\frac{\mathrm{i}}{4\pi}(\mathbf{g}^1\cdot\mathbf{x})(\mathbf{x}\cdot\mathbf{g}^2)}\sum_{n\in\mathbb{Z}}\mathrm{e}^{-\mathrm{i}n\mathbf{g}^2\cdot\mathbf{x}}\hat{h}(\mathbf{g}^1\cdot\mathbf{x}+2\pi n) \tag{C19}$$

The ordering of the lattice basis is arbitrary, so the most natural basis to expand h in would be a self-dual basis under Fourier transformation. Such a basis is provided by the eigenstates of the harmonic oscillator with a free parameter τ in the complex upper half plane. They take the form of the Hermite functions $h_{\tau,N}(x) = H_N\left(\sqrt{\frac{\tau}{2\pi\mathrm{i}}}x\right)\mathrm{e}^{\mathrm{i}\frac{\tau}{4\pi}x^2}$, where H_N is the Nth Hermite polynomial. Under Fourier transform we find

$$\hat{h}_{\tau,N}(y) = \frac{\mathrm{i}^N}{2\pi}H_N\left(\sqrt{\frac{\mathrm{i}}{2\pi\tau}}y\right)\mathrm{e}^{-\mathrm{i}\frac{1}{4\pi\tau}y^2} = \frac{\mathrm{i}^N}{2\pi}h_{-1/\tau,N}(y) \tag{C20}$$

The corresponding wavefunctions are closely related to the Jacobi theta function $\theta(u,\tau) = \sum_{n\in\mathbb{Z}}\mathrm{e}^{\mathrm{i}\pi n^2\tau+\mathrm{i}nu}$ (with

periods $2\pi, 2\pi\tau$). In particular for $h_{\tau,0}$:

$$\sum_{n\in\mathbb{Z}} \mathrm{e}^{\mathrm{i}n\mathbf{g}^1\cdot\mathbf{x}}\mathrm{e}^{\mathrm{i}\frac{\tau}{4\pi}(\mathbf{g}^2\cdot\mathbf{x}+2\pi n)^2} \tag{C21}$$

$$= \sum_{n\in\mathbb{Z}} \mathrm{e}^{\mathrm{i}\pi\tau n^2+\mathrm{i}n\mathbf{x}\cdot(\mathbf{g}^1+\tau\mathbf{g}^2)+\mathrm{i}\frac{\tau}{4\pi}(\mathbf{g}^2\cdot\mathbf{x})^2} \tag{C22}$$

$$= \theta\left(\mathbf{x}\cdot(\mathbf{g}^1+\tau\mathbf{g}^2);\tau\right)\mathrm{e}^{\mathrm{i}\frac{\tau}{4\pi}(\mathbf{g}^2\cdot\mathbf{x})^2} \tag{C23}$$

Since the complex numbers come with a natural metric, a choice for the free parameter τ amounts to picking a metric on the plane. We complexify coordinates using the map:

$$z = \frac{\ell_B}{\sqrt{2\pi\,\mathrm{Im}\,\tau}}\mathbf{x}\cdot(\mathbf{g}^1+\tau\mathbf{g}^2) \tag{C24}$$

Under this map $a_1 = \ell_B\sqrt{\frac{2\pi}{\mathrm{Im}\,\tau}}$ and $a_2 = \ell_B\tau\sqrt{\frac{2\pi}{\mathrm{Im}\,\tau}}$, so the area of the unit cell is

$$\frac{1}{2}|a_1\bar{a}_2 - \bar{a}_1 a_2| = \frac{\ell_B^2\pi}{\mathrm{Im}\,\tau}|\tau-\bar{\tau}| = 2\pi\ell_B^2 \tag{C25}$$

To convert from ϕ to $\mathbf{k}$ in the wavefunction, recall the minus sign of equation (C6). First consider $\phi_1 = \phi_2 = 0$ which corresponds to a corner of Brillouin zone:

$$\Theta(z;\tau) = \mathrm{e}^{\frac{\mathrm{i}}{4\pi}[(\mathbf{g}^1+\tau\mathbf{g}^2)\cdot\mathbf{x}]\mathbf{g}^2\cdot\mathbf{x}}\theta\left(\mathbf{x}\cdot(\mathbf{g}^1+\tau\mathbf{g}^2);\tau\right) \tag{C26}$$

$$= \mathrm{e}^{\mathrm{i}z\,\mathrm{Im}\,z/2\ell_B^2}\theta\left(\frac{\sqrt{2\pi\,\mathrm{Im}\,\tau}}{\ell_B}z;\tau\right) \tag{C27}$$

To center the wavefunction in the Brillouin zone translate it by $\mathbf{a}_1/2+\mathbf{a}_2/2$ to obtain

$$\langle\mathbf{x}|\mathbf{k}=\mathbf{0}\rangle \propto \mathrm{e}^{\frac{\mathrm{i}}{4}(\mathbf{g}^1-\mathbf{g}^2)\cdot\mathbf{x}}\Theta(z+a_1/2+a_2/2) \tag{C28}$$

$$\propto \sigma(z)\mathrm{e}^{-|z|^2/4\ell_B^2} \tag{C29}$$

where $\sigma(z)$ is the holomorphic (modified) Weierstrass sigma function[44] of Λ. The $\mathbf{k}\neq\mathbf{0}$ case can be constructed by similar translations:

$$\langle\mathbf{x}|\mathbf{k}\rangle = \mathcal{N}\mathrm{e}^{-\frac{1}{4\ell_B^2}|z-\mathrm{i}\ell_B^2 k|^2+\frac{\mathrm{i}}{2}\mathbf{k}\cdot\mathbf{x}}\sigma(z-\mathrm{i}\ell_B^2 k) \tag{C30}$$

$$= \mathcal{N}\mathrm{e}^{-\frac{1}{4}(\ell_B^{-2}|z|^2+\ell_B^2|k|^2-2\mathrm{i}\bar{k}z)}\sigma(z-\mathrm{i}\ell_B^2 k) \tag{C31}$$

where $\mathcal{N}$ is a $\mathbf{k}$ independent normalization constant whose value is not important. In fact $\langle\mathbf{x}|\mathbf{k}\rangle$ is the lowest Landau level wavefunction on a torus.

1. Higher Landau levels and form factors

Another way of understanding the construction is to consider an operator that commutes with $\hat{t}(\mathbf{a}_{1,2})$, and split the $\mathbf{k}$ sector by the spectrum of this operator. A natural choice is the kinetic energy $\boldsymbol{\pi}^2$. The nth level of $\boldsymbol{\pi}^2$ is the nth Landau level. Let $z = x+\mathrm{i}y$ and define the corresponding Wirtinger derivatives $\partial z = 1; \bar{\partial}z = 0$. In terms of these, the complexified kinetic and guiding center momenta take the form

$$\pi = -2\mathrm{i}\partial + \frac{\mathrm{i}\bar{z}}{2\ell_B^2}; \qquad \tilde{\pi} = \pi - \frac{\mathrm{i}\bar{z}}{\ell_B^2}. \tag{C32}$$

They satisfy the commutation relations

$$[\pi,\pi^\dagger] = -2\ell_B^{-2} \qquad [\tilde{\pi},\tilde{\pi}^\dagger] = 2\ell_B^{-2} \tag{C33}$$

where all other commutators vanish. After a $\sqrt{2}\ell_B^{-1}$ rescaling they therefore form two independent harmonic oscillator algebras. Furthermore $\boldsymbol{\pi}^2 = \pi\pi^\dagger + 2\ell_B^{-2}$, so we are in effect studying the harmonic oscillator. Note that $\pi^\dagger$ annihilates holomorphic functions multiplying the Gaussian $\mathrm{e}^{-\ell_B^{-2}|z|^2/4}$ of which the wavefunction $\langle\mathbf{r}|\mathbf{k}\rangle$ is an example. The general Hermite functions from before are precisely the states that can be found by applying π to $|\mathbf{k}\rangle = |n=0,\mathbf{k}\rangle$, namely

$$|n,\mathbf{k}\rangle = \frac{\ell_B^n\pi^n}{\sqrt{2^n n!}}|\mathbf{k}\rangle \tag{C34}$$

We use the guiding center translations to change momentum sectors:

$$|n,\mathbf{k}\rangle = \mathrm{e}^{\ell_B^2(\bar{k}\tilde{\pi}^\dagger - k\tilde{\pi})/2}|n,\mathbf{0}\rangle = \hat{t}(\mathbf{k}_\perp)|n,\mathbf{0}\rangle \tag{C35}$$

hence the action of the translation operators becomes

$$\hat{t}(\mathbf{k}_1^\perp)|n,\mathbf{k}_2\rangle = \mathrm{e}^{\frac{\ell_B^2}{4}(\bar{k}_1k_2-\bar{k}_2k_1)}|n,\mathbf{k}_1+\mathbf{k}_2\rangle \tag{C36}$$

Noting the Bloch-condition, we deduce boundary conditions for the wavefunctions

$$|n,\mathbf{k}+\mathbf{g}^i\rangle = \mathrm{e}^{\frac{\ell_B^2}{4}(\bar{k}g^i-\bar{g}^ik)}\hat{t}((\mathbf{g}^i)^\perp)|n,\mathbf{k}\rangle \tag{C37}$$

$$= -\mathrm{e}^{\frac{\ell_B^2}{4}(k\bar{g}^i-g^i\bar{k})}|n,\mathbf{k}\rangle \tag{C38}$$

This basis is very suitable for numerical calculations. The position operator takes the form $z = \mathrm{i}\ell_B^2(\pi^\dagger-\tilde{\pi}^\dagger)$ and $\bar{z} = \mathrm{i}\ell_B^2(\tilde{\pi}-\pi)$. This implies that the plane wave operator factorizes

$$\mathrm{e}^{\mathrm{i}\mathbf{q}\cdot\mathbf{x}} = \mathrm{e}^{\ell_B^2(q\pi-\bar{q}\pi^\dagger)/2}\mathrm{e}^{\ell_B^2(\bar{q}\tilde{\pi}^\dagger-q\tilde{\pi})/2} \tag{C39}$$

Denote the canonical displacement operator

$$D_m^n(\alpha) = \langle n|\mathrm{e}^{\alpha a^\dagger-\bar{\alpha}a}|m\rangle \tag{C40}$$

$$= \mathrm{e}^{-|\alpha|^2/2}\begin{cases}\sqrt{\frac{n!}{m!}}\alpha^{m-n}L_n^{(m-n)}(|\alpha|^2) & m\geq n\\ \sqrt{\frac{m!}{n!}}\bar{\alpha}^{n-m}L_m^{(n-m)}(|\alpha|^2) & n\geq m\end{cases}$$

where $L_b^{(a)}(x)$ are the associated Laguerre polynomials. With this in hand, suppose $\mathbf{q} = \mathbf{k}_1-\mathbf{k}_2+\mathbf{G}$ for some reciprocal lattice vector $\mathbf{G}\in\Lambda^\star$. Then the form factor takes the easily computable form:

$$\langle n,\mathbf{k}_1|\mathrm{e}^{\mathrm{i}\mathbf{q}\cdot\mathbf{x}}|m,\mathbf{k}_2\rangle \tag{C41}$$

$$= D_m^n(q\ell_B/\sqrt{2})\mathrm{e}^{\mathrm{i}\ell_B^2\mathbf{q}\wedge\mathbf{k}_2/2}\langle 0,\mathbf{k}_1|0,\mathbf{k}_1+\mathbf{G}\rangle \tag{C42}$$

$$= D_m^n(q\ell_B/\sqrt{2})\eta_{\mathbf{G}}\mathrm{e}^{\mathrm{i}\ell_B^2\mathbf{q}\wedge\mathbf{k}_2/2+\mathrm{i}\ell_B^2\mathbf{G}\wedge\mathbf{k}_1/2} \tag{C43}$$

where $\eta_{\mathbf{G}}$ is the parity of the reciprocal lattice vector such that $\eta_{\mathbf{G}} = 1$ if $\mathbf{G} \in 2\Lambda^\star$ and -1 otherwise. We use these matrix elements for numerical computation involving $\tilde{H}$. To do this note that $\psi^\alpha_{n\mathbf{k}}(\mathbf{r})$ obeys the Bloch periodicity $\psi^\alpha_{n\mathbf{k}}(\mathbf{r}+\mathbf{R}) = \mathrm{e}^{\mathrm{i}(\mathbf{k}+\mathbf{q}_\alpha)\cdot\mathbf{R}}\psi^\alpha_{n\mathbf{k}}(\mathbf{r})$. Factoring out the LLL wavefunction with crystal momentum $\mathbf{k}$ means that $\bar{\chi}$ transforms as $\chi^\alpha(\mathbf{r}+\mathbf{R}) = -\mathrm{e}^{\mathrm{i}\mathbf{q}_\alpha\cdot\mathbf{r} - \mathrm{i}\ell_B^{-2}\mathbf{R}\wedge\mathbf{r}/2}\chi^\alpha(\mathbf{r})$ – it obeys the magnetic translation symmetry with opposite chirality to $\langle\mathbf{r}|\mathbf{k}\rangle$. Note the invariance of the algebra under the relabeling $\pi \to \tilde{\pi}^\dagger$ and $\pi^\dagger \to \tilde{\pi}$. From this we can reuse the earlier matrix elements, by expanding $\chi^\alpha(\mathbf{r}) = \sum_{\bar{n}} c_{n\alpha}\langle\mathbf{r}|\overline{n\mathbf{q}_\alpha}\rangle$, where $|\overline{n\mathbf{k}}\rangle$ are the Landau levels of opposite chirality. In particular we define them by the properties $t(\mathbf{a}_i)|\overline{n\mathbf{q}_\alpha}\rangle = -\mathrm{e}^{\mathrm{i}\mathbf{a}_i\cdot\mathbf{q}_\alpha}|\overline{n\mathbf{q}_\alpha}\rangle$, $|\overline{n\mathbf{q}_\alpha}\rangle = \ell_B^n(\tilde{\pi}^\dagger)^n|\overline{\mathbf{q}_\alpha}\rangle/\sqrt{2^n n!}$, and $\langle\mathbf{r}|\overline{\mathbf{k}}\rangle = \overline{\langle\mathbf{r}|-\mathbf{k}\rangle}$. Including a spinor label we have basis states $|\overline{n\mathbf{k}}\alpha\rangle$. The matrix elements

$$\frac{1}{2M}\langle\overline{n\mathbf{q}_\alpha}|\tilde{\pi}\tilde{\pi}^\dagger|\overline{m\mathbf{q}_\alpha}\rangle = (n+1)\omega_c\delta^n_m\,, \tag{C44}$$

while for a potential of the form $V^\alpha_\beta(\mathbf{r}) = \sum_{\mathbf{G}} V^\alpha_\beta(\mathbf{G})\mathrm{e}^{\mathrm{i}(\mathbf{G}+\mathbf{q}_\alpha-\mathbf{q}_\beta)\cdot\mathbf{r}}$ (for some $\mathbf{q}_\alpha, \mathbf{q}_\beta$ which displace the Brillouin zones of the internal states) we have

$$\begin{aligned}
&\langle\overline{n\mathbf{q}_\alpha}\alpha|\hat{V}|\overline{m\mathbf{q}_\beta}\beta\rangle \qquad\qquad (\text{C45})\\
&\quad= \sum_{\mathbf{G}} V^\alpha_\beta(\mathbf{G})\langle\overline{n\mathbf{q}_\alpha}|\mathrm{e}^{\mathrm{i}(\mathbf{G}+\mathbf{q}_\alpha-\mathbf{q}_\beta)\cdot\mathbf{r}}|\overline{m\mathbf{q}_\beta}\rangle\\
&\quad= \sum_{\mathbf{G}} V^\alpha_\beta(\mathbf{G})\eta_{\mathbf{G}} D^{n\alpha}_{m\beta}(\mathbf{G})\,\mathrm{e}^{-\mathrm{i}\ell_B^2\left[\mathbf{G}+\frac{\mathbf{q}_\alpha-\mathbf{q}_\beta}{2}\right]\wedge\left[\frac{\mathbf{q}_\alpha+\mathbf{q}_\beta}{2}\right]}\\
D^{n\alpha}_{m\beta}(\mathbf{G}) &= D^n_m\left([\bar{G}+\bar{q}_\alpha-\bar{q}_\beta]\ell_B/\sqrt{2}\right)\,.
\end{aligned}$$

For comparison between the optimal ideal and true wavefunctions we find it most convenient to find the latter by solving (27). To do this we need the matrix elements of $\hat{\zeta}_{\mathbf{k}}$ which are

$$\begin{aligned}
&\langle\overline{n\mathbf{q}_\alpha}|\hat{\zeta}_{\mathbf{k}}|\overline{m\mathbf{q}_\alpha}\rangle \qquad\qquad (\text{C46})\\
&= -\omega_c\sum_{\mathbf{G}\neq\mathbf{0}} G^{-1}\mathrm{e}^{\mathrm{i}\ell_B^2\mathbf{G}\wedge\mathbf{k}}\langle\overline{n\mathbf{q}_\alpha}|\mathrm{e}^{\mathrm{i}\mathbf{G}\cdot\mathbf{r}}\tilde{\pi}^\dagger|\overline{m\mathbf{q}_\alpha}\rangle\\
&= -\omega_c\sqrt{2(m+1)}\sum_{\mathbf{G}\neq\mathbf{0}}\frac{\mathrm{e}^{\mathrm{i}\ell_B^2\mathbf{G}\wedge(\mathbf{k}-\mathbf{q}_\alpha)}}{\ell_B G}\eta_{\mathbf{G}} D^n_{m+1}(\bar{G}\ell_B/2)\,.
\end{aligned}$$

Using these pieces we can reproduce the same spectrum from $\tilde{H}+\hat{\zeta}_{\mathbf{k}}$ as from a plane-wave expansion of the original Hamiltonian. In practice we truncate the single-particle space to include the first 100 Landau levels.

2. Trace violation for the nth Landau level

We claimed in the main text that the trace violation for the nth Landau level is $2n$, which can be succinctly shown using the technology we have developed so far in this Appendix. The Bloch wavefunctions of the lowest Landau level take the form

$$\begin{aligned}
u_{0\mathbf{k}}(\mathbf{r}) &= \mathrm{e}^{-\mathrm{i}\mathbf{k}\cdot\mathbf{r}}\langle\mathbf{r}|\mathbf{k}\rangle \qquad (\text{C47})\\
&= N\mathrm{e}^{-\frac{1}{4}(\ell_B^{-2}|z|^2+\ell_B^2|k|^2)-\mathrm{i}k\bar{z}/2}\sigma(z-\mathrm{i}\ell_B^2 k)\,. \qquad (\text{C48})
\end{aligned}$$

Except for the Gaussian $\mathrm{e}^{-\ell_B^2|k|^2/4}$, this is holomorphic in k. The nth Landau level Bloch wavefunction can be similarly computed by noting that $\mathrm{e}^{-\mathrm{i}\mathbf{k}\cdot\mathbf{r}}\pi = (\pi+\bar{k})\mathrm{e}^{-\mathrm{i}\mathbf{k}\cdot\mathbf{r}}$, hence

$$|u_{n\mathbf{k}}\rangle = \frac{(\pi+\bar{k})^n}{2^{n/2}\sqrt{n!}}\mathrm{e}^{-\mathrm{i}\mathbf{k}\cdot\mathbf{r}}|\mathbf{k}\rangle\,, \tag{C49}$$

from which it is immediately clear that

$$\partial_{\bar{k}}|u_{n\mathbf{k}}\rangle = \ell_B\sqrt{\frac{n}{2}}|u_{n-1\mathbf{k}}\rangle - \frac{\ell_B^2 k}{4}|u_{n\mathbf{k}}\rangle\,. \tag{C50}$$

The Berry curvature is uniform for each Landau level:

$$\begin{aligned}
\Omega(\mathbf{k}) &= 2\partial_k\langle u_{n\mathbf{k}}|\partial_{\bar{k}}u_{n\mathbf{k}}\rangle - 2\partial_{\bar{k}}\langle u_{n\mathbf{k}}|\partial_k u_{n\mathbf{k}}\rangle \qquad (\text{C51})\\
&= 4\partial_k\langle u_{n\mathbf{k}}|\partial_{\bar{k}}u_{n\mathbf{k}}\rangle \qquad (\text{C52})\\
&= -\ell_B^2\,. \qquad (\text{C53})
\end{aligned}$$

We see that it is always negative and results in Chern number $\mathcal{C} = -1$. The corresponding trace violation is straightforwardly computed as

$$\begin{aligned}
\mathrm{Tr}\,g + \Omega &= 4\langle\partial_k u_{n\mathbf{k}}|\left(1-|u_{n\mathbf{k}}\rangle\langle u_{n\mathbf{k}}|\right)|\partial_{\bar{k}}u_{n\mathbf{k}}\rangle \qquad (\text{C54})\\
&= 2n\ell_B^2\langle u_{n-1\mathbf{k}}|u_{n-1\mathbf{k}}\rangle \qquad (\text{C55})\\
&= 2n\ell_B^2\,. \qquad (\text{C56})
\end{aligned}$$

Hence $(2\pi)^{-1}\int \mathrm{d}\mathbf{k}(\mathrm{Tr}\,g+\Omega) = 2n$ as claimed.

3. Circular dichroism criteria

A natural alternative to the trace condition as a measure of proximity to ideality relates to the null vectors of the quantum geometric tensor $q^{ab}(\mathbf{k}) = g^{ab}(\mathbf{k}) + \mathrm{i}\epsilon^{ab}\Omega(\mathbf{k})/2$. For ideal bands (with sufficient rotational symmetry) either $w_a = (\mathbf{e}_x + \mathrm{i}\mathbf{e}_y)_a/\sqrt{2}$ or its complex conjugate $\bar{w}_a$ are null-vectors of q^{ab} for all $\mathbf{k}$. Consider measuring the magnitude

$$\begin{aligned}
||q^{ab}w_b||^2 &= \left(g^{ab}\bar{w}_b - \frac{\mathrm{i}\epsilon^{ab}\bar{w}_b\Omega}{2}\right)\left(g^{ac}w_c + \frac{\mathrm{i}\epsilon^{ac}w_c\Omega}{2}\right)\\
&= \frac{1}{4}(\Omega - \mathrm{Tr}\,g)^2 + \frac{1}{4}(\mathrm{Tr}\,g)^2 - \det g\,. \qquad (\text{C57})
\end{aligned}$$

Using $\frac{1}{4}(\mathrm{Tr}\,g)^2 \geq \det g$ and taking $\Omega < 0$ we find

$$\begin{aligned}
\frac{||q\bar{w}||^2}{||qw||^2} &= \frac{(\mathrm{Tr}\,g+\Omega)^2 + [(\mathrm{Tr}\,g)^2 - 4\det g]}{(\mathrm{Tr}\,g-\Omega)^2 + [(\mathrm{Tr}\,g)^2 - 4\det g]} \qquad (\text{C58})\\
&\geq \left(\frac{\mathrm{Tr}\,g+\Omega}{\mathrm{Tr}\,g-\Omega}\right)^2\,, \qquad (\text{C59})
\end{aligned}$$

or in short

$$\frac{\sqrt{2\,\mathrm{Tr}\,g(\mathrm{Tr}\,g+\Omega)}}{\mathrm{Tr}\,g-\Omega}\geq\frac{||q\bar{w}||}{||qw||}\geq\frac{\mathrm{Tr}\,g+\Omega}{\mathrm{Tr}\,g-\Omega}\,. \tag{C60}$$

Ignoring the covariance of the denominator and the numerator, and to leading order in the trace violation, the average of this ratio can be approximately bounded

$$\sqrt{\frac{T}{2|\mathcal{C}|}}\gtrsim\int\frac{\mathrm{d}\mathbf{k}}{2\pi\ell_B^{-2}}\frac{||q\bar{w}||}{||qw||}\gtrsim\frac{T}{2|\mathcal{C}|}\,. \tag{C61}$$

Whenever the trace violation is small, so too must this average ratio be, but precise numerical comparison between the two quantities is not possible. This makes direct comparison between the deviation from ideality cited in [45] with the trace violations we quote practically difficult, though qualitatively they show similar features. For example, it monotonically increases in the nth Landau level

$$\frac{||q\bar{w}||}{||qw||}=\frac{n}{n+1} \tag{C62}$$

though the rate is much gentler than the trace condition.

Appendix D: Fourier expansion of $\hat{\zeta}$

In the main text we claimed the following identity regarding the periodic completion of the Weierstrass ζ function[44]

$$\hat{\zeta}(z)=\zeta(z)-\bar{z}/2\ell_B^2=-\mathrm{i}\sum_{\mathbf{G}\neq\mathbf{0}}\frac{\mathrm{e}^{\mathrm{i}\mathbf{G}\cdot\mathbf{r}}}{\ell_B^2 G}\,. \tag{D1}$$

The most straightforward derivation is to consider the anti-holomorphic derivative of this function:

$$\bar{\partial}(\zeta-\bar{z}/2\ell_B^2)=\pi\sum_{\mathbf{R}\in\Lambda}\delta^2(\mathbf{r})-1/2\ell_B^2 \tag{D2}$$

where the Dirac comb follow from the pole locations of ζ. The Dirac comb can be Fourier expanded, showing that

$$\bar{\partial}\hat{\zeta}=\frac{1}{2\ell_B^2}\sum_{\mathbf{G}\neq\mathbf{0}}\mathrm{e}^{\mathrm{i}\mathbf{G}\cdot\mathbf{r}}\,. \tag{D3}$$

Periodicity implies that there is a Fourier expansion with coefficients $c_{\mathbf{G}}$ of $\hat{\zeta}$

$$\hat{\zeta}(z)=\sum_{\mathbf{G}}c_{\mathbf{G}}\mathrm{e}^{\mathrm{i}\mathbf{G}\cdot\mathbf{r}} \tag{D4}$$

hence taking derivatives of this expression and matching terms we find $\mathrm{i}Gc_{\mathbf{G}}/2=1/2\ell_B^2$ for $\mathbf{G}\neq\mathbf{0}$. Since $\hat{\zeta}(z)$ has vanishing average, the claimed Fourier expansion follows.

Appendix E: Polarizability of Alkali Atoms

For completeness, let us derive the polarizability of alkali-metal atoms in the ground state. We label the internal atomic states, including the excited states by α. In the dipole approximation, an external electric field of strength $\mathbf{E}(t)=\sum_\omega\mathbf{E}_\omega\mathrm{e}^{-\mathrm{i}\omega t}$ modifies the Hamiltonian by

$$\delta H=-\mathbf{d}\cdot\mathbf{E}(t)=\sum V_\beta^\alpha(\omega)\mathrm{e}^{-\mathrm{i}\omega t}\left|\alpha\right\rangle\left\langle\beta\right| \tag{E1}$$

where $V_\beta^\alpha(\omega)=-\mathbf{d}_\beta^\alpha\cdot\mathbf{E}_\omega$. If the internal levels are governed by a reference Hamiltonian $H_0=\sum\omega_\alpha\left|\alpha\right\rangle\left\langle\alpha\right|$, the perturbation in the H_0 rotating frame becomes

$$\delta H^{\mathrm{rot}}=\sum_{\alpha\beta\omega}V_\beta^\alpha(\omega)\mathrm{e}^{-\mathrm{i}(\omega-\omega_\alpha+\omega_\beta)t}\left|\alpha\right\rangle\left\langle\beta\right|\,. \tag{E2}$$

To recast this as a static problem, we use a time-dependent Schrieffer-Wolff transformation $\left|\psi\right\rangle=\mathrm{e}^{-S(t)}\left|\tilde{\psi}\right\rangle$ where

$$S(t)=-\sum_{\alpha\beta\omega}\frac{V_\beta^\alpha(\omega)\mathrm{e}^{-\mathrm{i}(\omega-\omega_\alpha+\omega_\beta)t}}{\omega-\omega_\alpha+\omega_\beta}\left|\alpha\right\rangle\left\langle\beta\right|\,. \tag{E3}$$

Let $H_{\mathrm{atom}}=\sum E_\alpha\left|\alpha\right\rangle\left\langle\alpha\right|$ be the true atomic Hamiltonian absent driving, and pick H_0 so that $|E_\alpha-\omega_\alpha|\ll|\omega_\alpha-\omega_\beta|$ for all $\alpha\neq\beta$ that are coupled. To second order in $\mathbf{E}$, the time evolution of $\left|\tilde{\psi}\right\rangle$ is governed by

$$H^{(2)}=\sum_\alpha(E_\alpha-\omega_\alpha)\left|\alpha\right\rangle\left\langle\alpha\right|+\delta H^{(2)} \tag{E4}$$

where corrections to from the Schrieffer-Wolff transformation to the atomic piece have been neglected due to the proximity between H_{atom} and H_0, and where

$$\delta H^{(2)}=-\frac{1}{2}\sum_{\alpha\beta\gamma\omega_1\omega_2}\left|\alpha\right\rangle\left\langle\beta\right|\mathrm{e}^{-\mathrm{i}(\omega_1+\omega_2-\omega_\alpha+\omega_\beta)t}\times\left[\frac{V_\gamma^\alpha(\omega_1)V_\beta^\gamma(\omega_2)}{\omega_1-\omega_\alpha+\omega_\gamma}-\frac{V_\gamma^\alpha(\omega_1)V_\beta^\gamma(\omega_2)}{\omega_2-\omega_\gamma+\omega_\beta}\right]\,. \tag{E5}$$

Whenever the resonance condition $\omega_1+\omega_2-\omega_\alpha+\omega_\beta=0$ is met, this results in a static term. We assume the rotating wave approximation where only these resonant terms are important, that is ignoring higher order light shifts and taking any off-resonant oscillations much faster than the dynamics of interest. Due to the reality of $\mathbf{E}(t)$, clearly $\mathbf{E}_{-\omega}=\bar{\mathbf{E}}_\omega$. Furthermore, we consider the situation where the energy splitting of the states of interest is much smaller than the frequencies ω, so that the only resonant contributions arise when $\omega_1<0<\omega_2$ or conversely, and by focusing on ground states furthermore neglecting the contribution to the polarizability from virtual levels formed below the ground state. Combining these considerations, the energy takes the form

$$\delta H^{(2)}=-\sum_{\omega_1,\omega_2>0,\mathrm{res}}\left|\alpha\right\rangle\left\langle\beta\right|\frac{(\bar{\mathbf{E}}_{\omega_1}\cdot\mathbf{d}_\gamma^\alpha)(\mathbf{E}_{\omega_2}\cdot\mathbf{d}_\beta^\gamma)}{\omega_\gamma-\omega_2-\omega_\beta} \tag{E6}$$

$$=-\sum_{K,q}(-)^{K-q}\alpha^{K,-q}[\bar{E}(\omega_1)\otimes E(\omega_2)]^{K,q} \tag{E7}$$

where in the last line, we have transformed to the spherical tensor basis with $K = 0, 1, 2$ corresponding to scalar, vector, and tensor polarizabilities. This picture is particularly clear when the lifetimes of all states are infinite so that H_{atom} is Hermitian. Unfortunately this is not true for the excited states where the imaginary part $\operatorname{Im} E_\alpha = -\Gamma_\alpha/2$ measures the line-width. To account for this H_0 should include the linewidth for states which are not resonant, so that $\omega_\alpha \mapsto \omega_\alpha - \mathrm{i}\Gamma_\alpha/2$ is complex. The mismatch between the true and reference energies $E_\alpha - \omega_\alpha$ functions as a species-dependent chemical potential due to the lasers being off-resonant.

1. Spherical tensor decomposition

The electrons in the atom have orbital angular momentum $\mathbf{L}$, under which $\mathbf{d}$ is a vector operator, as well as spin angular momentum $\mathbf{S}$. When the atomic reference Hamiltonian H_0 is rotationally symmetric, eigenstates carry definite angular momentum $\mathbf{J} = \mathbf{L} + \mathbf{S}$. Consider a degenerate manifold of excited states γ with definite angular momentum J_γ, coupling to ground states with angular momentum J. We can work out the $K = 0, 1, 2$ polarizabilities using the Wigner-Eckart theorem, which is to say using the SU(2) representation theory. We use the convention that the reduced matrix elements of a spherical tensor is related to the $3j$ symbol as follows:

$$\langle J_1 m_1 | T^{Kq} | J_2 m_2 \rangle = (-)^{J_1 - m_1} \langle J_1 || T^K || J_2 \rangle \begin{pmatrix} J_1 & K & J_2 \\ -m_1 & q & m_2 \end{pmatrix}$$

and that the tensor product of spherical tensors takes the form (where $[J] = 2J + 1$)

$$[A \otimes B]^{Kq} = \sum_{m_{a,b}} \sqrt{[K]} (-)^{K-q} \begin{pmatrix} 1 & 1 & K \\ m_a & m_b & -q \end{pmatrix} A^{m_a} B^{m_b} \tag{E8}$$

A tedious but straightforward calculation then shows that

$$\begin{aligned}
\langle J m_\alpha | \alpha^{K,q} | J m_\beta \rangle &= \sqrt{[K]} \sum_\gamma (-)^{m_a + m_b} \begin{pmatrix} 1 & 1 & K \\ -m_a & -m_b & q \end{pmatrix} \frac{\langle J m_\alpha | d_{m_a} | J_\gamma m_\gamma \rangle \langle J_\gamma m_\gamma | d_{m_b} | J m_\beta \rangle}{\omega_\gamma - \omega} \\
&= \sqrt{[K]} \sum_\gamma (-)^{m_a + m_b - m_\alpha + m_\gamma} \frac{|\langle J || \mathbf{d} || J_\gamma \rangle|^2}{\omega_\gamma - \omega} \begin{pmatrix} 1 & 1 & K \\ -m_a & -m_b & q \end{pmatrix} \begin{pmatrix} J & 1 & J_\gamma \\ -m_\alpha & m_a & m_\gamma \end{pmatrix} \begin{pmatrix} J_\gamma & 1 & J \\ -m_\gamma & m_b & m_\beta \end{pmatrix} \\
&= \sqrt{[K]} \sum_\gamma (-)^{J_\gamma - m_\alpha} \frac{|\langle J || \mathbf{d} || J_\gamma \rangle|^2}{\omega_\gamma - \omega} \begin{Bmatrix} J & J & K \\ 1 & 1 & J_\gamma \end{Bmatrix} \begin{pmatrix} J & J & K \\ m_\beta & -m_\alpha & q \end{pmatrix}
\end{aligned} \tag{E9}$$

Hence the reduced matrix elements of the polarizability take the form

$$\langle J || \alpha^K || J \rangle = \sum_\gamma \sqrt{[K]} (-)^{J_\gamma - J} \frac{|\langle J || \mathbf{d} || J_\gamma \rangle|^2}{\omega_\gamma - \omega} \begin{Bmatrix} J & J & K \\ 1 & 1 & J_\gamma \end{Bmatrix} \tag{E10}$$

Of particular interest to the alkali metals is the $J = 1/2$ case, which represents the ground state

$$\langle 1/2 || \alpha^K || 1/2 \rangle = \sum_\gamma \frac{|\langle 1/2 || \mathbf{d} || J_\gamma \rangle|^2}{\omega_\gamma - \omega} \times \begin{cases} \frac{1}{\sqrt{6}} & K = 0 \\ -\frac{11 - 4J_\gamma(J_\gamma+1)}{8\sqrt{3}} & K = 1 \end{cases} \tag{E11}$$

$$= \sum_\gamma \frac{|\langle 1/2 || \mathbf{d} || J_\gamma \rangle|^2}{\omega_\gamma - \omega} \times \begin{cases} \frac{\langle 1/2 || 1 || 1/2 \rangle}{2\sqrt{3}} & K = 0 \\ \frac{11 - 4J_\gamma(J_\gamma+1)}{12\sqrt{2}} \mathrm{i} \langle 1/2 || \mathbf{J} || 1/2 \rangle & K = 1 \end{cases} \tag{E12}$$

To rewrite this in the usual form, we note that with our convention

$$[\bar{\mathbf{E}}(\omega_1) \otimes \mathbf{E}(\omega_2)]^{Kq} = \begin{cases} \frac{\bar{\mathbf{E}}(\omega_1) \cdot \mathbf{E}(\omega_2)}{\sqrt{3}} & K = 0 \\ \frac{[\bar{\mathbf{E}}(\omega_1) \times \mathbf{E}(\omega_2)]_q}{\sqrt{2}} & K = 1 \end{cases} \tag{E13}$$

For alkali metals, the dominant sources of polarizability are the $D_{1,2}$ lines connecting the ground state $S_{1/2}$ to the $P_{1/2,3/2}$ levels at energy $\omega_{1/2,3/2}$, where $\langle S_{1/2} | \mathbf{d} | P_{3/2} \rangle = \sqrt{2} \langle S_{1/2} | \mathbf{d} | P_{1/2} \rangle = \sqrt{2} d$. Hence the second order Hamiltonian takes the form

$$\delta H^{(2)} = -\sum_{\gamma, \omega_{1,2}\text{ res}} \frac{|\langle S_{1/2} || \mathbf{d} || J_\gamma \rangle|^2}{\omega_\gamma - \omega} \left[\frac{\bar{\mathbf{E}}(\omega_1) \cdot \mathbf{E}(\omega_2)}{6} + \frac{\mathrm{i}(11 - 4J_\gamma(J_\gamma+1)) \mathbf{J} \cdot [\bar{\mathbf{E}}(\omega_1) \times \mathbf{E}(\omega_2)]}{24} \right] \tag{E14}$$

$$= \sum_{\omega_{1,2}\text{ res}} \frac{d^2 \bar{\mathbf{E}}(\omega_1) \cdot \mathbf{E}(\omega_2)}{6} \left[\frac{1}{\omega - \omega_{1/2}} + \frac{2}{\omega - \omega_{3/2}} \right] + \frac{\mathrm{i} d^2 \mathbf{J} \cdot \bar{\mathbf{E}}(\omega_1) \times \mathbf{E}(\omega_2)}{3} \left[\frac{1}{\omega - \omega_{1/2}} - \frac{1}{\omega - \omega_{3/2}} \right]. \tag{E15}$$

The most important feature is that the vector polarizability from the two lines destructively add when far detuned. In this regime, when $\omega \ll \omega_{1/2}, \omega_{3/2}$ or $\omega \gg \omega_{1/2}, \omega_{3/2}$, we find

$$\alpha_V \to \frac{d^2(\omega_{3/2} - \omega_{1/2})}{3(\omega - \omega_{1/2})^2}. \tag{E16}$$

As discussed, the imaginary part of the polarizability can be obtained by $\omega_{1/2,3/2} \to \omega_{1/2,3/2} - \mathrm{i}\Gamma/2$. When far detuned the imaginary part of the scalar potential scales in the same way as α_V, namely

$$\mathrm{Im}\alpha_S \to \frac{d^2\Gamma}{4(\omega - \omega_{1/2})^2}. \tag{E17}$$

Element	Li	Na	K	Rb	Cs
$\Gamma/2\pi$ MHz	5.9	9.8	6.0	5.9	4.9
$(\omega_{3/2} - \omega_{1/2})/2\pi$ THz	0.01	0.52	1.7	7.1	16.6
$\mathrm{Im}\,\alpha_S/\alpha_V \times 10^4$	4	0.1	0.03	0.006	0.003

TABLE II. Key spectral features of $D_{1,2}$ lines in alkali metals. Splitting data from [65–70] and lifetime data from [71, 72]. At the stated precision the isotope shift is negligible, and we have quoted the average Γ for the two lines. The quoted ratio $\mathrm{Im}\,\alpha_S/\alpha_V$ is the asymptotically approached ratio in the far detuned regime.

The ratio of these two quantities is a key Fig. of merit for the lifetime of alkali metals in OFLs

$$\frac{\mathrm{Im}\alpha_S}{\alpha_V} \to \frac{3\Gamma}{4(\omega_{3/2} - \omega_{1/2})}. \tag{E18}$$

In particular, given some fixed non-scalar potential, no detuning will give lower heating than that suggested by taking this ratio to its asymptotic value. In practice it is a good estimate so long as ω is a multiple of $\omega_{3/2} - \omega_{1/2}$ from resonance. This figure of merit explains why heavy alkali-metals are preferable, as the fine structure splitting $\omega_{3/2} - \omega_{1/2}$ is a relativistic effect that increases with atomic number. We quote the relevant values in Table II.